Acta Materialia 314 (2026) 122337

Contents lists available at ScienceDirect

Acta Materialia

journal homepage: www.elsevier.com/locate/actamat

Full length article

Redox-mediated sustainable solid-state synthesis of NiTi: An *in situ* study of alloying pathways and phase evolution mechanisms

Lennart Hitzemann, Shao Lou Wei *, Stefan Zaefferer, Dierk Raabe *

Max Planck Institute for Sustainable Materials, 40237 Düsseldorf, Germany

ARTICLE INFO

Keywords:
Metal-hydrogen systems
Phase stability
In situ characterization
Thermokinetic analysis

ABSTRACT

NiTi shape memory alloys serve in advanced biomedical and electro-mechanical devices. However, conventional liquid metallurgical fabrication of NiTi from primary Ni and Ti is energy and emission intensive. Here, we present a sustainable one-step approach to produce NiTi from NiO and TiH_2 in the solid state. It involves the decomposition of TiH_2 and the reduction of NiO, with concurrent diffusion-based alloy formation. The reaction kinetics were examined by thermogravimetric analysis and *in situ* synchrotron X-ray diffraction. The results show that the decomposition, reduction, and alloying behavior of the system are influenced by the hydrogen partial pressure. Based on these findings, we have developed design guidelines to increase the NiTi-phase yield, resulting in a bulk sample containing up to 33.7 vol.% of NiTi which exhibits the desired thermoelastic martensitic transformation. The findings of this work also provide fundamental insights into sustainable fabrication of application-worthy NiTi alloys fully in the solid-state.

1. Introduction

In the context of climate change, reducing societal carbon footprint has become an emerging global priority [1,2]. Metallurgical synthesis and processing, which accounts for nearly 40% of total industrial greenhouse gas emissions and >10% of global energy consumption, provide a huge lever on transitioning towards cleaner products [3–5], circular material flows [6–8], and near-net-zero emission manufacturing [9,10]. Although Fe and Al constitute the major share of engineering structural alloys in use [9], the associated energy costs and CO_2 equivalent emissions (30.8 MJ/kg; 2.1 kg/kg CO_2e for Fe [11], and 183 MJ/kg; 13.3 kg CO_2e/kg for Al [11]) are, per mass produced, substantially below those of Ni and Ti, which, their roles as critical elements in aerospace [12], biomedical [13], and automotive [14] applications, carry significantly higher environmental impacts of 290 MJ/kg plus 22 kg CO_2e/kg (for Ni) [11], and 685 MJ/kg plus 17.0–46.5 kg CO_2e/kg (for Ti) [15,16], respectively. This discrepancy not only underscores the need for lower carbon emission metal extraction routes [9], but equally important, less energy intensive thermomechanical pathways for microstructural design and modulation which define the properties [9]. Merging both quests into a single solid state operation, as suggested in this paper, brings chemical metallurgy closely together with physical metallurgy and microstructure research.

With Ni and Ti incorporated in near-equiatomic proportions, the prototypical nitinol alloys [17–20] attract broad attention due to their shape memory and superelastic properties [13,21]. However, the reliance on the two exceptionally energy- and carbon-intensive alloying elements positions this material class as a representative case where sustainability-oriented processing improvement and disruptive production pathways are urgently needed. Traditionally, NiTi alloys are fabricated by high-temperature melting and casting followed by sequential thermomechanical treatments to tailor composition and phase constitutions, thereby enabling the desired thermo-elastic martensitic transformation responses [13,20,22]. To address the high (energy-)cost stemming from liquid alloying, enable near-net shape fabrication, achieve a higher Ni content without segregation, and to create tailored microstructures [13,17,22–24], appreciable research efforts have been dedicated to powder metallurgical fabrication of NiTi alloys, leveraging conventional sintering [25,26] hot isostatic pressing (HIP) [27,28], spark plasma sintering [29,30], mechanical alloying, and metal injection molding (MIM) [13,17]. Additionally, additive manufacturing of NiTi alloys has been explored *via* selective laser sintering [13]. Powder metallurgical routes can, in principle, also be distinguished by the utilization of pre-alloyed or elemental powders.

Mentz et al. [23,31] showcased the fabrication of NiTi alloys with near theoretical mass density via MIM and HIP of gas-atomized pre

* Corresponding authors.
E-mail addresses: sl.wei@mpi-susmat.de (S.L. Wei), d.raabe@mpi-susmat.de (D. Raabe).

https://doi.org/10.1016/j.actamat.2026.122337
Received 9 December 2025; Received in revised form 6 April 2026; Accepted 10 May 2026
Available online 11 May 2026

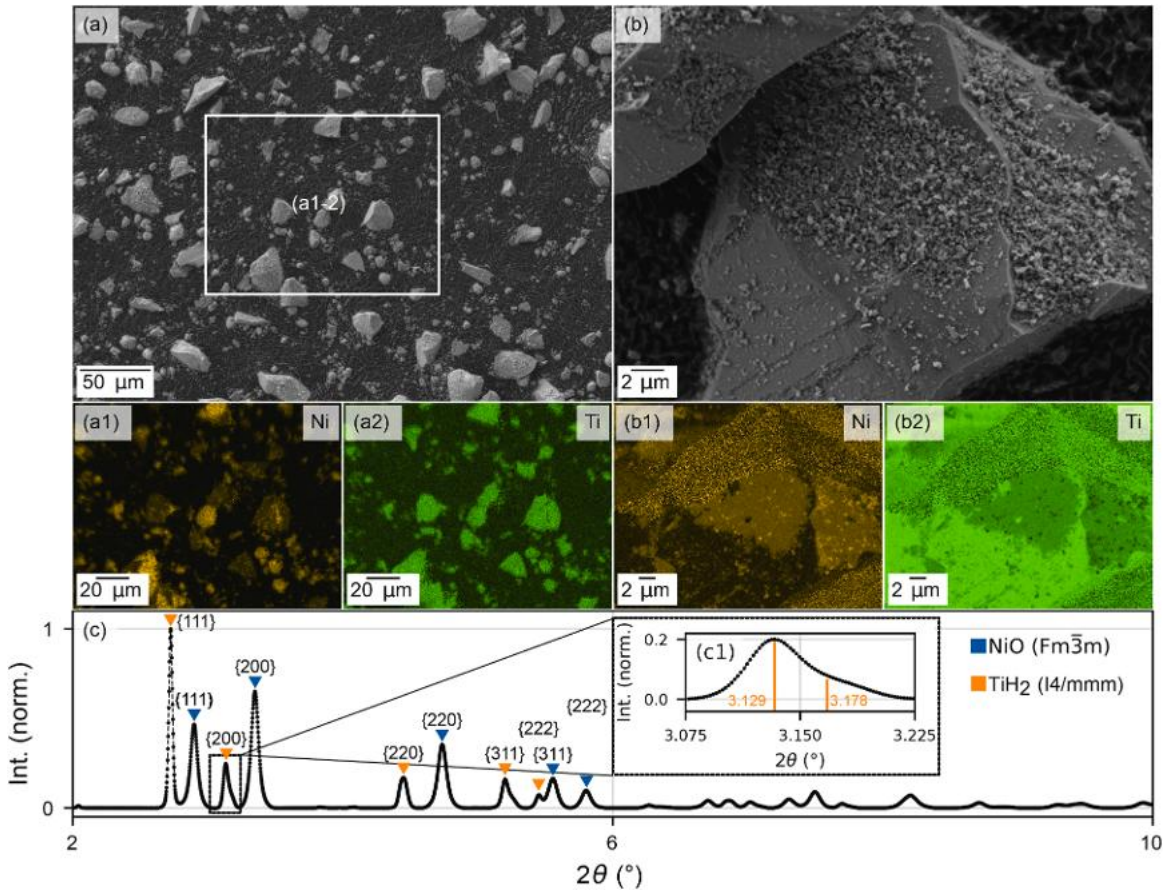

Fig. 1. Analysis of the initial NiO-TiH_2 powders prior to the synthesis treatment. (a-b) Secondary electron (SE) image of the NiO-TiH_2 powders. The powders were spread on copper tape for imaging. (a1-b2) Corresponding EDS mapping of Ni and Ti, the larger TiH_2 particles are covered by NiO. (c) SXRD spectrum of the NiO-TiH_2 powder. For better readability, the background has been subtracted. Inset of (c) reveals the asymmetric {200} peak shape of the TiH_2, indicating tetragonal distortion [44] arising from the face-centered tetragonal (FCT) structured ε-TiH_2-phase, by shortening of one lattice constant of the δ-TiH_2 phase.

alloyed NiTi. They revealed that the macroscopic mechanical performance is strongly influenced by the presence of O or C contamination, whose quantities accumulate throughout the process steps and are particularly elevated in finer powders. The Ti_2Ni intermetallic phase, with a complex face-centered cubic structure [32,33], tends to form in the inter-granular regions and trap most of the O impurities due to its higher solubility compared with the NiTi phase. As a result, the martensitic transformation temperature of the NiTi phase is often less affected, compared to the pure NiTi phase, as confirmed by differential scanning calorimetry measurements. It was also concluded that the deteriorated ductility is mostly ascribed to the apparent brittleness of the Ti_2Ni phase.

Zhu et al. [34] prepared porous NiTi alloys by mixing Ni- and Ti-elemental powders for 24 h, cold compaction (25–200 MPa), and sintering (8 h, 920–1000 °C). It was found that the material's strength revealed a noticeable increase at sintering temperatures beyond 940 °C, for which the mechanism was ascribed to the partial melting of the Ti_2Ni phase, promoting diffusion while alleviating stress concentrators. Additionally, they found that at a temperature of 920 °C, the diffusion rate of Ni and Ti is not sufficient to form large quantities of intermetallic Ni-Ti phases. Since the fusion of elemental Ni and Ti is exothermic [13, 22,35], thermal combustion and explosion synthesis of elemental Ni-Ti mixtures has also been studied [17,22]. Due to partial melting, capillary effects arise [13], which leads to a porous microstructure for elemental Ni-Ti powder blends [13,17,22,34]. A noteworthy distinction within the alloying of elemental Ni-Ti powder blends is mechanical alloying, as it creates pre-alloyed NiTi powder, without liquid state processing. Mousavi et al. [36] utilize high intensity ball milling of Ni and Ti under a protective Ar atmosphere. After 60 h of ball milling, nanocrystalline NiTi particles were observed. In a consecutive annealing step, intermetallic phases of Ti_2Ni and Ni_3Ti were also observed.

These findings all show that oxygen control of NiTi alloys prepared *via* powder metallurgy is challenging [13,17,22]. Also, formation of intermetallic phases (Ti_2Ni, Ni_3Ti) and increased porosity are important factors, affecting the amount of recoverable strain and the magnitude of the elastic modulus, when the sample is produced from elemental Ni-Ti. Although the utilization of pre-alloyed NiTi powder may be able to reduce the amount of impurities, and Ti_2Ni-, and Ni_3Ti-intermetallic phases, the gas-atomization process is preceded by a Ni-Ti melt, increasing energy demand. To achieve the overarching goal of a more sustainable single-step solid state alloying process, three main dilemmas need to be overcome, especially when elemental powders mixtures are exploited as feedstock: (1) fine Ti powder must be handled carefully during processing to avoid contamination, as its high surface-to-volume ratio promotes oxygen uptake; (2) Ti powder, resembling pre-alloyed NiTi powder, is produced by gas atomization, which often increases energy costs; and (3) adequate Ni–Ti particle contact is necessary for solid-state interdiffusion, rendering cold compaction of the green body critical.

In response to these limitations, a chemical metallurgy-inspired approach has emerged, where TiH_2 was exploited as a less reactive and less expensive elemental Ti precursor [24,25,37–40]. Since the reactivity of TiH_2 with oxygen is substantially below that of elemental Ti, the oxygen ingress is mitigated until thermal decomposition of TiH_2, enabling more homogenous and less contaminated NiTi microstructures [24,38]. This approach simultaneously enables physical

metallurgy-inspired elastic modulus modulation via the pore-forming effect resulting from the thermal decomposition of TiH_2, which can help minimize stress shielding in biomedical implant applications [13, 39]. The brittleness of TiH_2 [41] mitigates the sticking and agglomeration, commonly observed with ductile Ti particles, facilitating cold compaction and thereby the green body integrity [42]. In addition, TiH_2 powders offer lower cost and greater availability at tolerable impurity levels [38,41,42].

Notably, the hydrogen released during thermal decomposition of TiH_2 prompts reconsiderations of the Ni source. In this context, NiO becomes an attractive alternative since it can be readily reduced in an *in situ* manner, saving additional energy cost arising from the otherwise required preceding elementary Ni extraction process and reheating operation for alloying. In addition, the near equiatomic proportion of Ni and Ti in the targeted alloy implies that neither an additional reducing agent nor a thermomechanical treatment is necessary, since the theoretical pathway $NiO+TiH_2 \rightarrow NiTi+H_2O$ leverages an *one step feedstock-to-alloy* operation [2]. A more recent study [43] revealed the potential for phase transformation pathway modulation in NiTi alloys through interstitial hydrogen incorporation, underscoring the importance of controlling hydrogen partial pressure during synthesis along with the significance of integrating both physical and chemical metallurgy processes as well as their interconnections.

On the foregoing basis, three critical issues emerge that define the focus of the present study: (1) What is the suitable temperature range and gas atmosphere to encourage concurrent TiH_2 decomposition, *in situ* NiO reduction, and alloying? (2) What are the critical mass transport and phase transformation micro-events that govern the process? (3) To what extent can the resulting microstructure-property combinations approach those of NiTi alloys produced via conventional processing routes? Combing thermal gravimetry and *in situ* synchrotron X-ray diffractometry, we revealed the synthesis kinetics and mechanistic details of coupled TiH_2 decomposition, NiO reduction, and subsequent phase transformation pathways in pure Ar and 5 vol. % H_2 atmospheres. The resulting microstructures were evaluated utilizing scanning electron microscopy. Additionally, the characteristic austenite-martensite transition, required for shape recovery, was observed with differential scanning calorimetry.

2. Materials and methods

2.1. Pellet sample preparation for the synthesis

The NiO-TiH_2 powders used in this study as starting feedstock were mixed from NiO (Merck Chemicals GmbH, powder size: 0.5–6 μm) and TiH_2 (Thermo Fisher Scientific Inc., powder size: <44 μm) powders (See **Supplementary Table S1** for details) via a low-energy powder mixer for 3 h at 20 °C and cold compacted (~370 MPa) into disc-shaped samples with diameters of 6.35 mm and a mass of ~100 mg. The resulting samples were analyzed via scanning electron microscopy (SEM), energy dispersive X-ray spectroscopy (EDS), electron backscatter diffraction (EBSD) and synchrotron X-ray diffraction (SXRD). The TiH_2 particles with larger diameters are uniformly covered by the smaller NiO particles, as seen in the SEM and EDS micrographs (Fig. 1(a-b)). The SXRD spectrum further confirms that the prepared powder mixtures do not exhibit noticeable signs of impurities or mechanical alloying (Fig. 1(c)), except for a subtle rutile (TiO_2) peak. After Rietveld refinement the composition is identified as 59.8 wt.% NiO, 39.7 wt.% TiH_2 and 0.3 wt. % Rutile. The Rutile content was small enough to be neglected. A prominent asymmetric peak shape is present on the {200} reflection group for the TiH_2-phase (Fig. 1(c) inset), which is indicative of tetragonal distortion [44] arising from the face-centered tetragonal (FCT) structured ε-TiH_2-phase, by shortening of one lattice constant of the cubic δ-TiH_2 phase. The a and b lattice constants were determined as 4.4768±0.0004 Å with a smaller c constant of 4.4102±0.0004 Å. To account for possible variations in the hydrogen content of the TiH_2 phase, the following text uses δ-phase to denote TiH_x ($1 < x \leq 2$). The lattice constant of cubic NiO was determined as 4.1838±0.0004 Å.

2.2. Thermogravimetric analysis

To evaluate the conceived path of the one-step reactive alloying process in terms of reduction degree and reduction kinetics, several thermogravimetric analysis (TGA) experiments were performed using a DynTHERM-TGA instrument from Waters [45], utilizing furnace-heating. For all the samples, the pressure, total flow rate, holding time, and heating rate were kept consistent **(Supplementary Table S2)**, while the temperature and atmosphere were adjusted. The first set of experiments was conducted at 800 °C both with and without adding 5% H_2 to the atmosphere. In order to ensure reproducibility of the measurements the experiments were repeated three additional times **(Supplementary Fig. S2)**. In each experiment the gas concentration was designed using a total flow rate of 300 ml/min and ideal gas condition were assumed in the gas mixture. Because the SXRD experimental setup (Section 2.4) differs from the TGA setup described here, slight flow rate deviations are expected. For data analysis, the raw data were smoothed and interpolated, both utilizing the Python library SciPy, to enable the calculation of derivatives for the weight loss and conversion degree rate. A final validation experiment was performed, with parameters consistent to the previously described. The atmosphere was chosen to be Ar + 5% H_2 and the holding temperature was extended to 1150 °C.

2.3. Microstructural characterization

The samples were prepared for microstructural characterization, following the standard metallographic route, including hot embedding, grinding, and fine polishing down to 1 μm with SiC abrasive papers along with diamond suspension. As a final step, the samples were polished with oxide polishing suspension (OPS) and cleaned with water, soap, and ethanol.

Electron microscopy characterization was performed using a ZEISS Merlin high-resolution field-emission scanning electron microscope (FE-SEM).

For microstructure analysis of bulk samples, an acceleration voltage of 10–15 kV at 5–10 nA was used at a working distance varying from 10–15 mm. For a first overview on elemental composition of the samples EDS analysis was done based on K_α X-ray lines. The EBSD measurements were performed with an EDAX DigiView V camera and post-processed with spherical indexing provided by EDAX OIM software V9.1. Micrographs of the entire sample were stitched from several smaller scale micrographs of the sample. The sample holder and the embedding material were masked with Affinity Photo software package.

Considering the limited conductivity of the mixed powders, a 10 nm-thick carbon coating was deposited on them after being spread on a double-sided glue-coated copper tape. For elemental analysis with high lateral resolution the acceleration voltage was lowered down to 5 kV. As a result, the corresponding EDS characterization of Ni and Ti was conducted using the L_α lines.

2.4. In situ synchrotron X-ray diffraction analysis

Since the diffusion-based alloying does not affect the overall sample weight, it could not be observed directly in the TGA experiments. *In situ* SXRD was therefore exploited to study the quantitative and qualitative phase evolution during heating and holding to 800 °C in Ar and Ar + 5% H_2 **(Supplementary Table S3)**. The cold compacted sample (see Section 2.1) was placed inside a Bach heating device using a sample holder equipped with a thermocouple and a resistive heater **(Supplementary Fig. S1 (a))**. To ensure uninflected X-ray passage, the sample holder facilitated two holes at sample height, ensuring the incident beam could enter and leave the Bach heating device through two Kapton windows

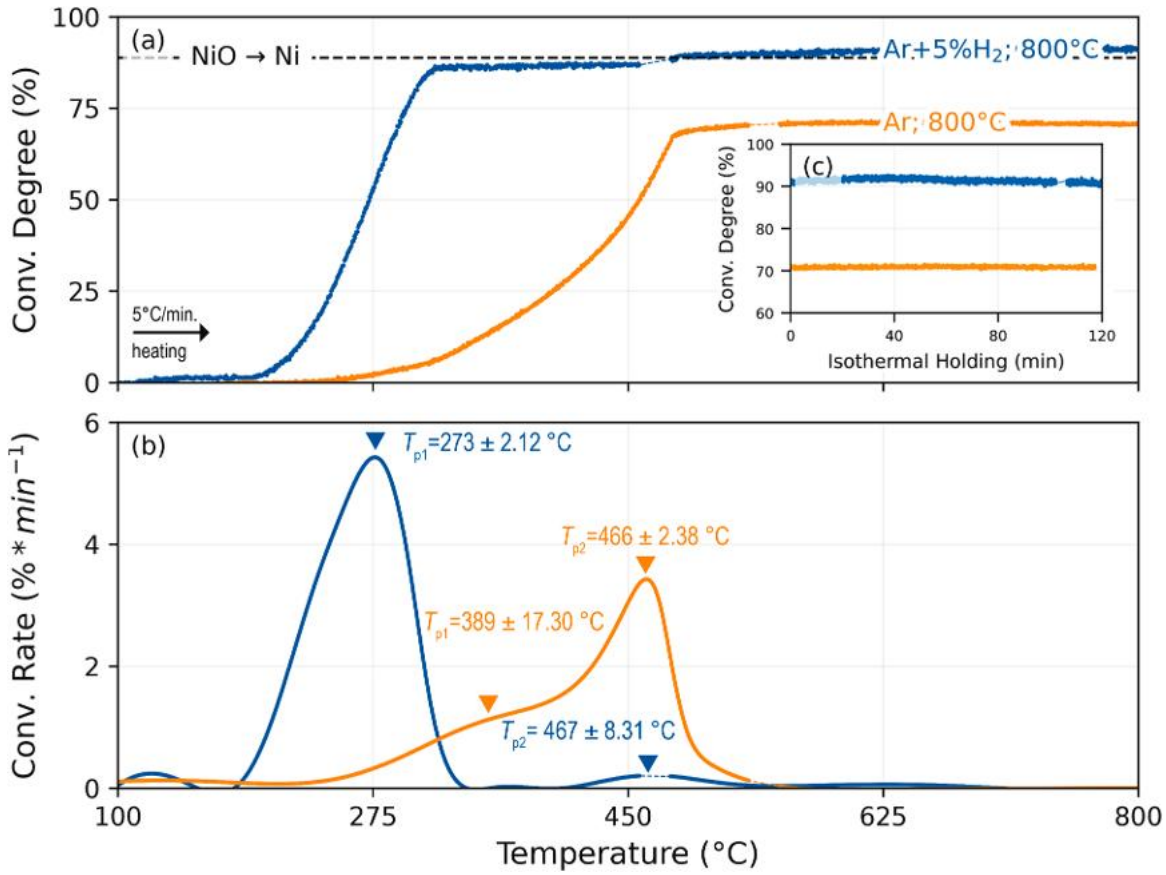

Fig. 2. Overall synthesis kinetics under different gas atmospheres. (a) Conversion curve of the sample calculated on the measured instantaneous mass loss. The dashed line denotes the theoretical conversion degree, representing complete reduction of NiO. (b) First derivative of the conversion degree curve. Peak positions are given as average with standard deviation from three additional experiments for each condition to ensure reproducible results (Supplementary Fig. S2 and S3). (c) Inset shows the evolution of the conversion degree during the 2 h of isothermal holding at 800 °C. The conversion degree does not change significantly, a slight oxidation can be observed at the Ar + 5% H_2 sample.

(Supplementary Fig. S1 (c)). The atmosphere was controlled by in- and outlet gas lines that transported the premixed atmosphere from a gas bottle through the device and out through the exhausts **(Supplementary Fig. S1 (b))**. The X-ray beam energy was chosen as 101.5 keV corresponding to a monochromatic wavelength of 0.12226 Å, which according to our previous experience ([2,46]), enabled an optimal balance between the spatial resolution and the number of accessible Debye-Scherrer rings. The raw diffractograms were captured every 10 s with a 2D-detector. For data analysis, the 2D-spectra underwent calibration and fast azimuthal integration utilizing PyFAI. Calibration was performed using a LaB_6 standard sample. The more detailed quantitative data analysis was carried out with Rietveld refinement in the MDI JADE software. For the refinement, the 1D spectrum was analyzed from 2° to 10° (2θ) and the background was fitted with a 9th order polynomial function. The JADE software allows for a batch analysis, where similar spectra can be individually refined with a source file, enabling the detailed tracking of phase formation and decomposition. To distinguish between ε- and δ-TiH_2 is difficult, since the only change in the XRD spectrum is the asymmetry of the peaks due to the tetragonal distortion of the unit cell. As the ε-phase gradually transforms to the δ-phase, the convoluted peaks could not be separated. Since the ε to δ transition occurs below 100 °C (read from phase diagram [47]), the distorted peaks were fitted with the δ-profile for Rietveld refinement throughout this work except for the composition analysis in Section 2.1, where a tetragonal standard pattern was used. Additionally, the same set of experiments has been repeated with a tenfold increased heating rate to obtain additional information about the influence of the heating rate **(Supplementary Table S1 and Supplementary Fig. S1- S10)**.

3. Results

3.1. Overall synthesis kinetics

The first set of synthesis experiments was conducted under continuous heating conditions in the TGA (5 °C/min heating rate), aiming to capture the overall conversion trend and resolve the critical kinetic phenomena that are at play. To evaluate the overall conversion trend, the conversion degree can be calculated according to Eq. (3.1), where the conversion degree α is the ratio of the current total mass loss m_{sample} of the sample in relation to the theoretical possible mass loss after full reduction and decomposition $\Delta m_{NiO+TiH_2 \rightarrow NiTi}$. Analog the conversion rate is the first derivative of the conversion degree α by time t (Eq. (3.2)).

$$\alpha(t) = \frac{\Delta m(t)}{\Delta m_{total}} = \frac{\Delta m_{sample}(t)}{\Delta m_{NiO+TiH_2 \rightarrow NiTi}} \tag{3.1}$$

$$\dot{\alpha}(t) = \frac{d\alpha(t)}{dt} \tag{3.2}$$

When heating in pure Ar, the conversion initiates at ~275 °C, followed by a noticeable increase, eventually saturating at ~70% conversion degree when the temperature reaches ~566 °C (Fig. 2(a)). As shown in Fig. 2(c), the conversion degree barely increases even after a prolonged isothermal holding period at 800 °C. Comparing the final conversion degree with the theoretical value corresponding to full NiO reduction (~87.5%, see the dashed black line in Fig. 2(a)), it is evident that the hydrogen released from the seemingly complete thermal decomposition of the δ-phase only contributes to partial oxide

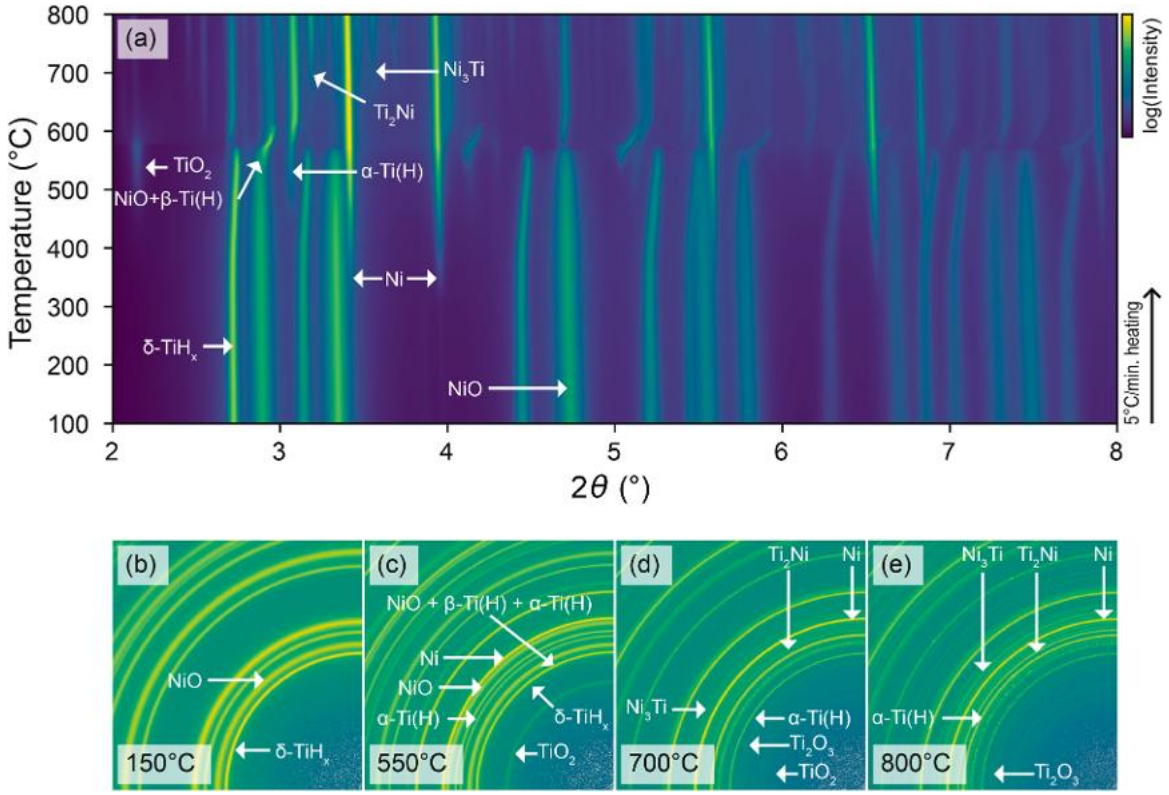

Fig. 3. *In situ* SXRD observations of the synthesis process in Ar. (a) Contour map of logarithmic intensity as a function of temperature. Noticeable phase transformations can be observed at 570 °C. (b-e) Cropped quarter of the 2D-detector image, the changes of the characteristic rings illustrate the phase evolution over temperature.

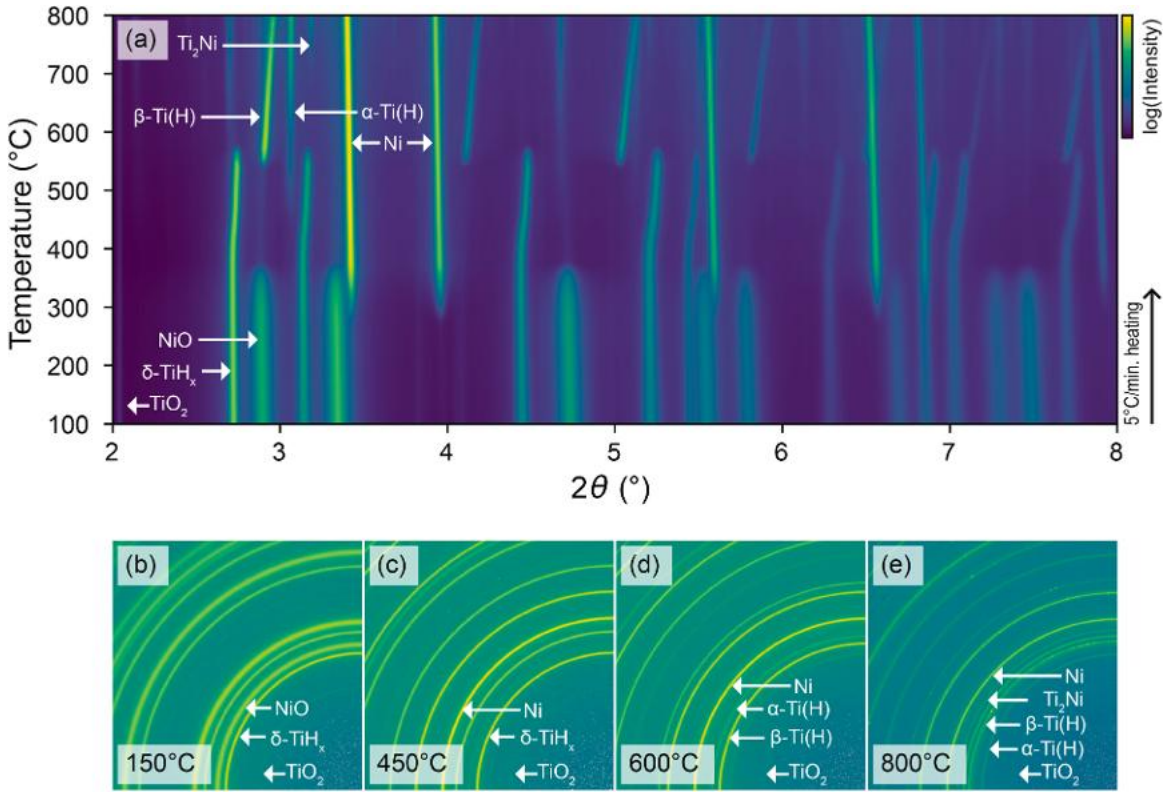

Fig. 4. *In situ* SXRD observations of the synthesis process in Ar + 5% H_2. (a) Contour map of logarithmic intensity as a function of temperature, where phase transformations start to occur ~280 °C. (b-e) Cropped quarter of the 2D-detector image, the changes of the characteristic rings illustrate the phase evolution over temperature.

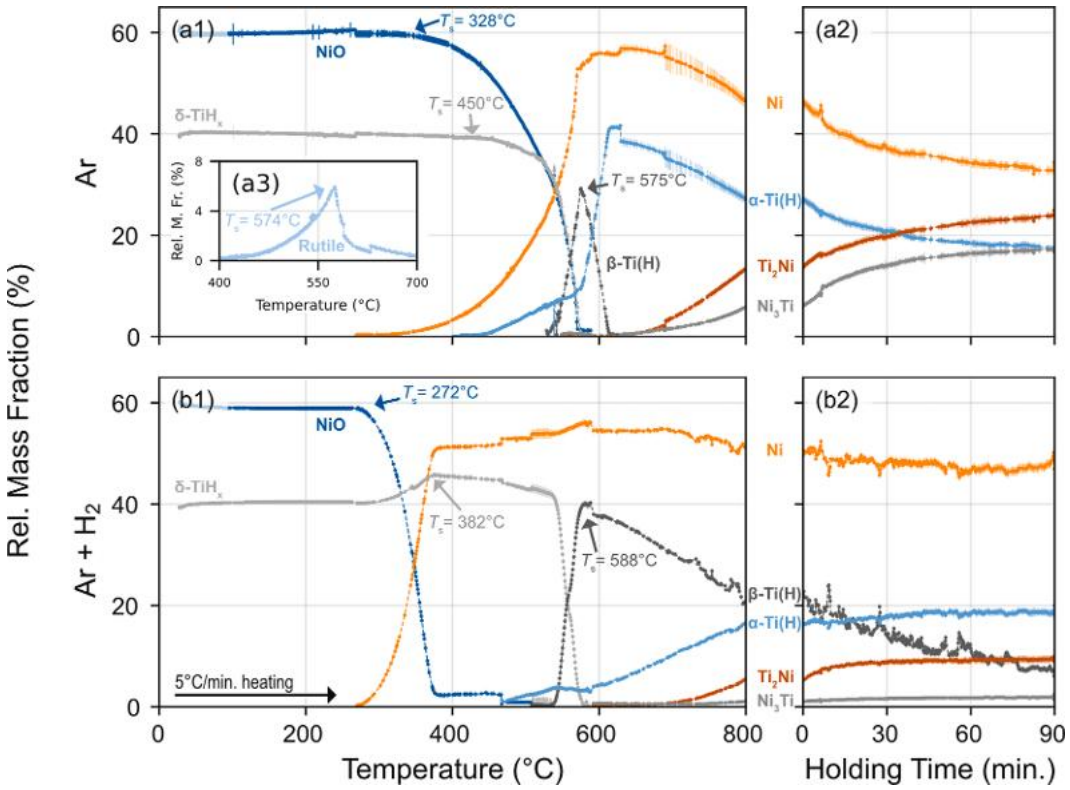

Fig. 5. Relative mass fraction evolution of phases during heating and holding. (a1-a3) relative mass fraction of phases during heating and holding at 800 °C in Ar. (b1 and b2) relative mass fraction of phases during heating and holding at 800 °C in Ar + 5% H_2.

reduction. By contrast, when 5% H_2 is introduced to the atmosphere, the conversion start temperature is lowered down to ~180 °C, accompanied by a much steeper increase up to ~86% when temperature only approaches 300 °C. The conversion degree reveals an asymptotic increasing trend when temperature further increases and eventually plateaus at 92% after imposing the same 2-h isothermal holding section at 800 °C.

To render the kinetic analysis more quantitative, the conversion rates were calculated (*i.e.* the first derivatives of the conversion degrees, Fig. 2 (b)), where multiple deconvoluted peaks are revealed, implying the activation of multistep hydride decomposition/oxide reduction microevents. At least two prominent peaks are seen in the pure Ar synthesis case, respectively locating at ~370 °C and ~463 °C. In the absence of any other reducing agent in this process, these two peaks suggest a multistep thermal decomposition process of the δ-phase, which is in line with the earlier literature [48]. A salient distinction in the peak position is seen when 5% H_2 is present: the first peak appears at ~276 °C, while the second peak instead remains at ~468 °C. These noticeable differences in the conversion responses underpin the pronounced dependency of the hydride decomposition/oxide reduction processes on the gas atmosphere as well as the potential interplay involved, which altogether motivates dedicated mechanistic explorations, as revealed next, starting with *in situ* SXRD investigations.

3.2. *In situ SXRD investigation of concurrent hydride decomposition, oxide reduction, and solid-state reactive alloying*

To further understand the hydride decomposition and oxide reduction micro mechanisms at play, as well as the conceived solid-state alloying pathway *via* diffusion, *in situ* SXRD experiments were performed at DESY. During continuous heating (5 °C/min heating rate) to 800 °C, contour maps are obtained after azimuthal integration. When heating in Ar, the first metallic Ni peak is observed at 328 °C (Fig. 3), indicating the onset of NiO reduction. The lattice parameters of Ni and NiO reveal similar changes as temperature increases: the diffraction peaks shift towards lower 2θ values, proving an increase in the lattice parameter mostly due to thermal expansion. At ~580 °C, no NiO peak can be observed any longer, suggesting the completion of NiO reduction through the hydrogen released from thermal decomposition of the δ-phase.

The decomposition of the δ-phase commences at 460 °C, when the first α-Ti(H) peak is observed. At ~500 °C, the δ-phase decomposes to β-Ti(H) in addition to α-Ti(H). Since the β-Ti phase is present under temperatures that are well below 882 °C (*i.e.* the β-transus for pure Ti) the role of solutionized hydrogen as a β-stabilizer is clearly visible. The suffix (H) is added to the α- and β-Ti phases since the lattice parameters and the phase stability are affected by the dissolved hydrogen, as will be revealed in more detail in the ensuing sections. With increasing temperature, the δ, α- and β-Ti(H) lattice constants all shift towards higher 2θ values, as their lattice parameter gradually shrinks due to the gradual loss of the initially interstitially solved hydrogen. After ~600 °C, this trend is inversed for α-Ti(H), as the lattice expands due to thermal expansion when no more hydrogen is leaving the interstitial sites.

Interestingly, at ~570 °C, the intensity of the TiO_2 peak increases, while the intensities of the δ-phase and NiO diffraction peaks simultaneously become smaller. This further underpins the presence of an alternative reduction mechanism, rivalling the H_2-based reduction of NiO in the same temperature regime. At higher temperatures (~625 °C), however, the intensity of the TiO_2 peak diminishes, suggesting the (partial)-reduction of this stable oxide phase, coinciding with the observations of Jiménez et al. [48]. Additionally, the intermetallic phases Ti_2Ni and Ni_3Ti become more prominent, confirming the onset of diffusion-driven reactive alloying.

When 5% H_2 is present in the atmosphere (Fig. 4), the onset of NiO reduction shifts towards lower temperatures (~280 °C) compared to the foregoing pure Ar case. Complete reduction of NiO is reached below 370 °C, suggesting that the hydrogen in the atmosphere serves as the major reductant, since the hydride decomposition incepts at a higher

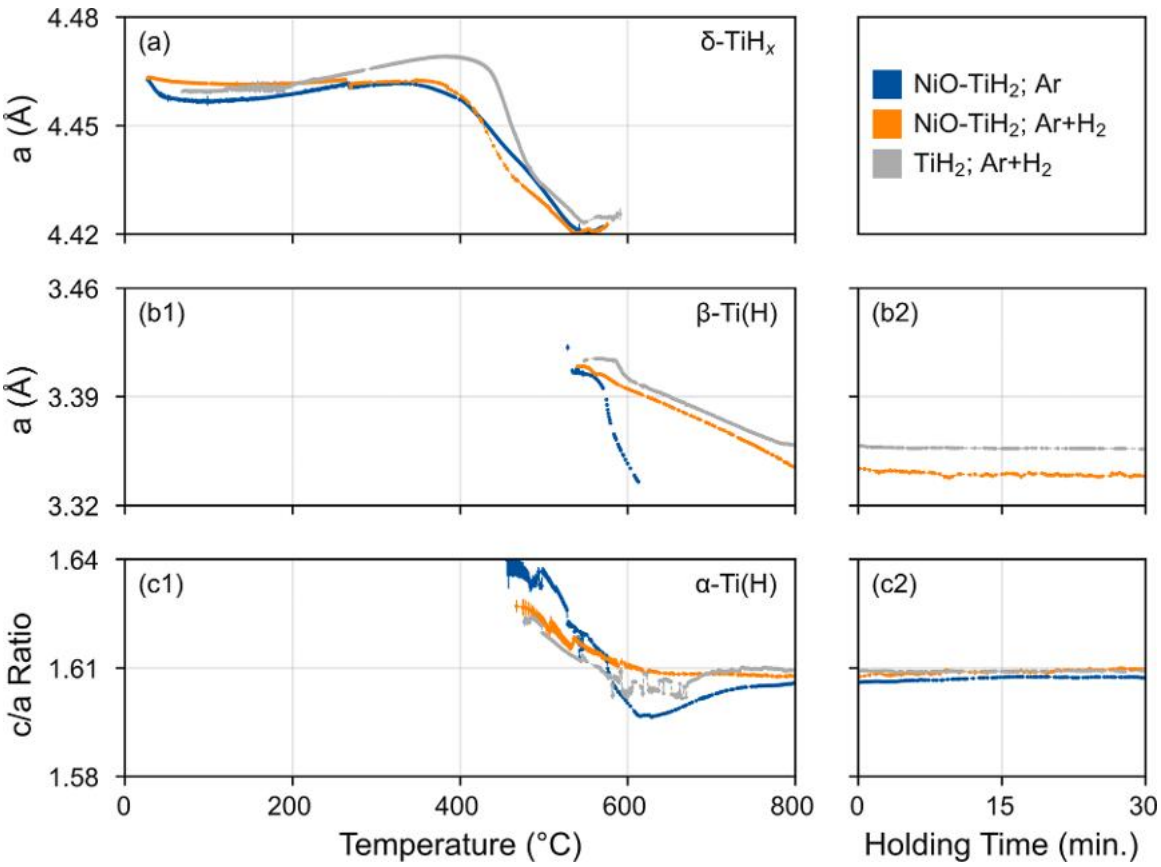

Fig. 6. Lattice constant evolution of δ, α- and β-Ti in Ar and Ar + 5% H_2. (a) evolution of the δ-phase lattice parameter during heating (b) evolution of the β-Ti(H) lattice constant during heating and isothermal holding at 800 °C (c) evolution of the α-Ti(H) c/a ratio during heating and isothermal holding. For comparison, the evolution of pure TiH_2 is also given, for which the experimental conditions were kept consistent during SXRD measurements.

temperature ~471 °C, as evidenced by the presence of α-Ti(H). β-Ti(H) starts to form at ~546 °C, with decreasing lattice constant as temperature increases. Compared to the pure Ar sample, the hydride decomposition tends to take place at higher temperature, probably due to the 5% H₂ in the atmosphere that changes the fugacity of hydrogen and thus promotes phase stability of hydrides as also suggested by the corresponding Pressure–Composition–Temperature (PCT) diagram [49]. In contrast to the hydride decomposition in pure Ar, β-Ti(H) is still present at 800 °C, which can also be rationalized by the increased phase stability in the hydrogen-enriched atmosphere. The lattice constant evolution trends of Ni, NiO, δ-phase, α-Ti(H) and β-Ti(H) behave similarly as the pure Ar sample, which will be revealed in quantitative depth in the subsequent sections. The onset of intermetallic Ni-Ti phase formation seems to be also shifted towards higher temperatures (~706 °C), where only the Ti_2Ni phase reveals a noticeable intensity.

Rietveld refinement was next performed to quantify the temperature-dependent phase fraction evolution during the foregoing two measurements, as comparatively shown in Fig. 5. To improve readability, results of all the Ti-O phases are provided in **Supplementary Fig. S6**. In Ar atmosphere, a discernible decrease of the NiO phase fraction starts at 328 °C. In combination with a decrease in the lattice parameter of the δ-phase (Fig. 6(a)) in a similar temperature range, it can be concluded that the δ-phase begins to release hydrogen at 322 °C, which consequently serves as the immediate reductant carrier responsible for NiO reduction. Despite the reduction of NiO, the relative phase fraction of the δ-phase remains unchanged up to 450 °C, suggesting that the hydrogen release in the 322–450 °C temperature range should solely be ascribed to the stoichiometric variation in the δ-phase. The reduction rate of NiO and the decomposition rate of the δ-phase seem to be coupled and decrease at a similar average rate (−0.2 wt.%/ °C and −0.22 wt.%/ °C, respectively). During δ-phase decomposition, the α-Ti(H) phase forms first followed by β-Ti(H), which was also observed by Jiménez et al. [48], implying a core-shell kinetic process of the δ-phase decomposition. Within the same temperature range and timescale, the transient rutile phase also forms (Fig. 5(a3)), underpinning an additional metallothermic reduction of NiO with Ti that might account for the lower conversion degree observed in the TGA with Ar. With increasing temperature, the rutile and β-Ti(H) relative phase fractions, however, begin to decrease at ~575 °C. The lattice parameter of β-Ti(H) decreases monotonically as solutionized hydrogen leaves the solid phase (Fig. 6 (b1)). At the end of the heating section and throughout the isothermal holding period the relative phase fractions of Ni and α-Ti(H) decrease with a similar average rate (−0.07 wt.%/ °C and −0.08 wt.%/ °C respectively), while those of the Ni-Ti intermetallic-phases (Ti_2Ni and Ni_3Ti) continue to increase (on average 0.08 wt.%/ °C and 0.04 wt.%/ °C respectively). The solid-state reactive alloying reveals an asymptotic response, as the conversion rate ceases to increase over the isothermal holding time (Fig. 5(a2)), leading to 24% and 17% relative fractions of Ti_2Ni and Ni_3Ti, respectively.

With 5% H_2 present in the atmosphere, the NiO reduction starts earlier at ~272 °C compared to the pure Ar case (Fig. 5(b1)). The lattice constant of the δ-phase begins to decrease at 356 °C, and the decomposition of the δ-phase shifts to higher temperatures (Fig. 6(a)). Since NiO is almost fully reduced before any discernible decrease in the relative δ-phase fraction, it can be concluded that the NiO reduction is achieved mainly by the presence of 5% H_2 in the atmosphere. Similar to the Ar case, the δ-phase first decomposes to α-Ti(H) at ~382 °C. When the temperature increases, the majority of the decomposition product becomes β-Ti(H), which incepts at a similar temperature of ~529 °C. The overall decomposition rate of the δ-phase, however, is slower

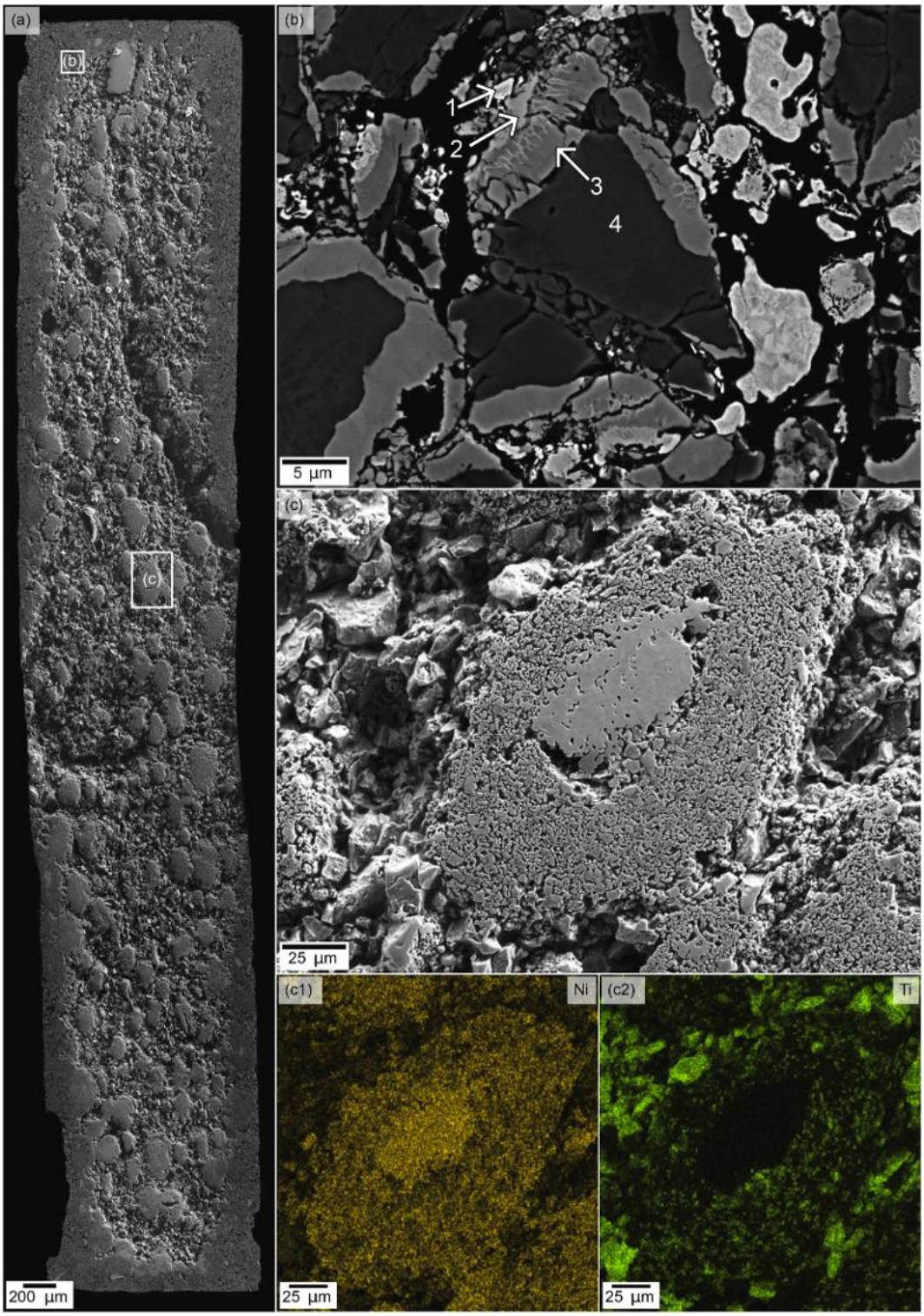

Fig. 7. Microstructure of the SXRD sample processed in Ar. (a) Overview of the sample cross-section, stitched from multiple secondary electron (SE)-images. (b) Characteristic particles in the sample edge (backscattered electron imaging (BSE)). Following the concentration gradient of Ni (Ti) from the outside to the inside, intermetallic phases of Ni_3Ti, NiTi and Ti_2Ni are present. (c) Characteristic Ni-rich elliptical particles (SE-imaging), with a Ni concentration gradient and pure Ni core, are spread over the sample.

compared to pure Ar (−0.22 *versus* −0.24 wt.%/ °C), as seen from Fig. 5. When 5% H_2 is present, NiO is reduced with −0.53 wt.%/ °C, indicating a faster reduction rate. In contrast, the δ decomposition rate does not change as significantly (−0.31 wt.%/ °C in Ar and −0.22 wt.%/ °C in Ar +5% H_2). This changes for the β-Ti(H) phase. In pure Ar, the thermal decomposition starts at 575 °C and is completed at 629 °C. With 5% H_2 present, the decomposition sets in at 588 °C and even when the sample reaches 800 °C, β-Ti(H) is still existent, indicating β-Ti(H) stabilizing ability of hydrogen. While heating, the relative phase fraction of β-Ti(H) decreases while α-Ti(H) is increasing, suggesting decomposition of β-Ti (H) to α-Ti(H). During the holding period, the relative phase fraction of β-Ti(H) is still decreasing, however the relative phase fraction of α-Ti(H)

Table 1
EDS measurements of microstructure in pure Ar.

Spot	Ni (at.%)	Ti (at.%)	O (at.%)
1	79.9 ± 3.1	5.6 ± 4.0	14.5 ± 9.5
2	43.5 ± 3.2	48.8 ± 2.5	7.7 ± 11.1
3	28.0 ± 4.0	60.1 ± 2.6	11.9 ± 13.7
4	0.8 ± 9.6	92.5 ± 2.2	6.7 ± 12.3

remains constant. Between 700–750 °C, the intermetallic phases Ni_3Ti and Ti_2Ni begin to form, while the overall Ni and Ti (α, β) relative phase fractions continue to decrease. During isothermal holding at 800 °C, the relative phase fractions of Ni_3Ti and Ti_2Ni develop asymptotic behaviors, respectively reaching 2 and 9 wt.% after 90 min. As mentioned previously, the hydride decomposition has long been conceived to follow a core-shell model, indicating a difference between the sample core and edge. In addition, the formation of titanium oxides in the sample center would serve to confirm any metallothermic reaction between NiO and Ti. These hypothesized thermal decomposition and reduction micro-events are expected to become visible also in terms of corresponding microstructure changes between the sample core and edge, thus motivating dedicated microstructure analyses of the samples.

3.3. Microstructures of the specimens analyzed by SXRD

To gain further insights into the distribution of the observed phases and localizes specific mechanisms including oxidation and diffusion-driven reactive alloying, detailed microstructure analyses of the SXRD samples were performed. The sample tested in pure Ar atmosphere can

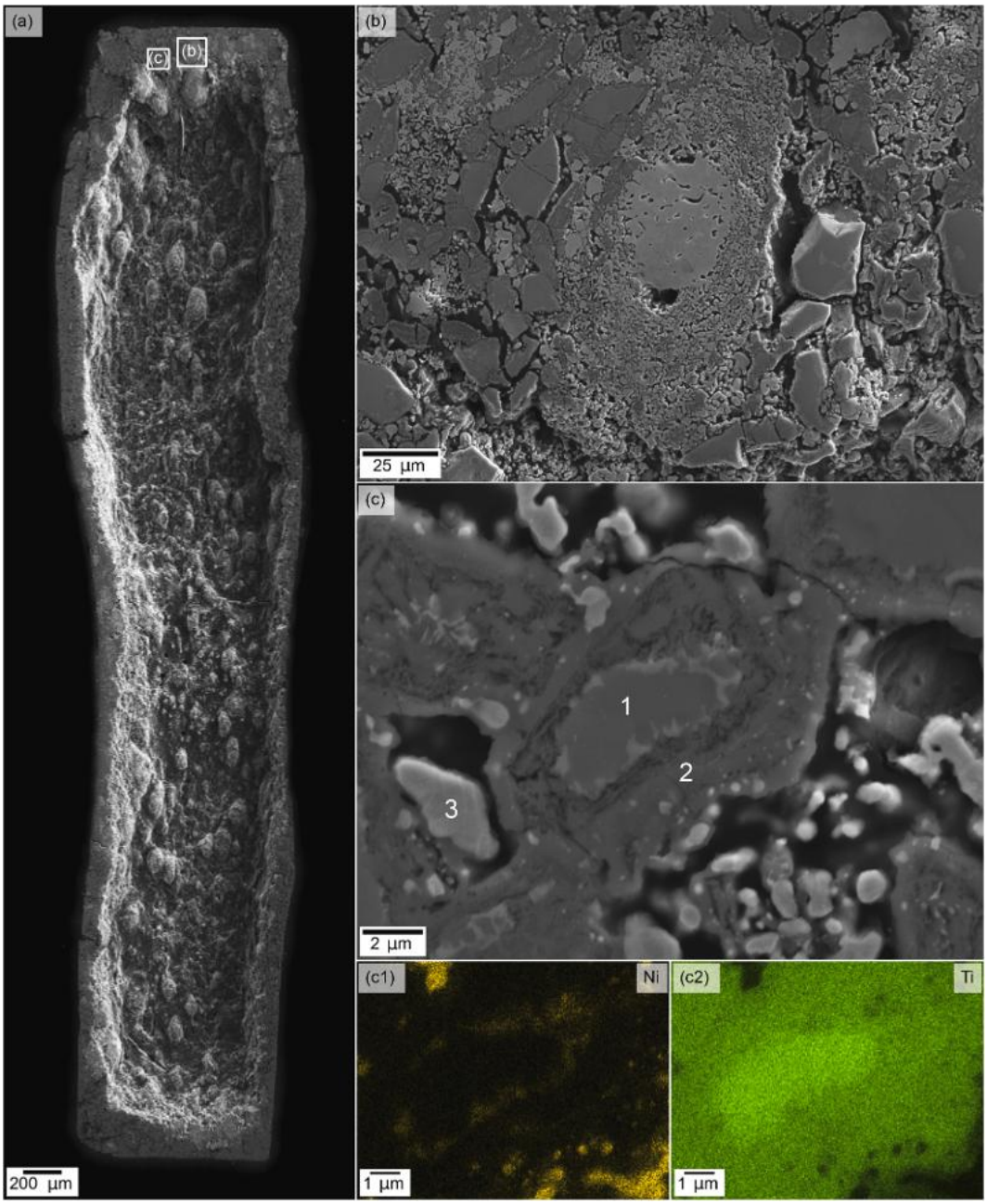

Fig. 8. Microstructure of the SXRD sample processed in Ar + 5% H_2. (a) Overview of the sample cross-section, stitched from multiple secondary electron (SE)-images. (b) Similar to the pure Ar sample, elliptical particles enriched in Ni form all over the sample. (c) Characteristic particles in the sample edge (SE-imaging). Ni (Ti) concentration gradient between Ni rich and Ti rich zone is observed. The Ti rich area shows high concentrations of oxygen corresponding to TiO and TiO_2.

Table 2
EDS measurement of the *in situ*SXRD specimen tested in an Ar + 5% H_2 atmosphere.

Spot	Ni (at.%)	Ti (at.%)	O (at.%)
1	0.7 ± 16.1	68.3 ± 2.2	31.0 ± 11.3
2	3.7 ± 4.3	34.9 ± 2.2	61.5 ± 10.6
3	83.0 ± 3.1	3.3 ± 5.0	13.7 ± 9.4

be divided into two zones, edge and core, clearly visible in the cross-sectional view (Fig. 7(a)). While the entire sample is porous, the sample edge appears to be denser than the sample center. According to EDS measurements **(Supplementary Fig. S5)**, the edge region is depleted in Ni and enriched with Ti.

Elliptical particles enriched in Ni spread over the entire sample (core and edge) (Fig. 7(c)). The solid particle core consists of Ni, surrounded by a Ni and Ti containing shell (Fig. 7(c1–2)). This shell in turn consists of smaller particles, similar to Fig. 7(b). A typical Ni-Ti containing particle in the sample edge (Fig. 7(b)) shows a clear concentration gradient of Ni content from the outside towards the inside according to EDS measurements (Table 1). The fishnet structure on the particle outside was too fine and exceeds the resolution limit of EDS. The observation of Ni-gradients (Fig. 7(b)) with stoichiometric compositions of Ni (1), NiTi (2), Ti_2Ni (3) and Ti (4) support the proposed diffusion-driven solid-state reactive alloying.

The observed change in microstructure from the sample rim towards its core indicates that different mechanisms may be at play during reduction and hydride decomposition, depending on the specific observation range selected between sample center and edges.

Similar to the microstructure obtained from pure Ar exposure, in the presence of 5% H_2, the microstructure varies between the sample edge and center (Fig. 8(a)). The edge is denser than the center. The sample edge consists of particles similar to Fig. 7(c), a Ni rich core surrounded by smaller particles containing Ni and Ti (Fig. 8(c)). A gradient of Ni concentration was measured from the outside towards the inside with EDS (Table 2, Fig. 8(c1–2)). The Ti gradient is reversed. Similar to the pure Ar sample, a fishnet-like structure is present around the Ti rich core. According to EDS measurements, the oxygen content of the Ti-rich phase is elevated compared to the Ar case (Table 2). While the oxygen content of the Ni rich phase is comparable to the Ar case, the Ti rich phases are enriched with oxygen and approach the stoichiometry of TiO_2 on the particle edge (Fig. 8(c) spot 2) and TiO (Fig. 8(c) spot 1) in the particle center. It seems that the selective oxidation of Ti is much more pronounced, even when additional hydrogen is present in the atmosphere.

4. Discussion and rationalization of the observations

4.1. Interplay amongst hydride thermal decomposition, oxide reduction, and solid-state reactive alloying

4.1.1. Role of the gas atmosphere on hydride decomposition

The conceived one-step process of solid-state reactive alloying of NiTi can be separated into three critical kinetic processes: hydride thermal decomposition, NiO reduction, and solid-state alloying. As the decomposition of hydrides provides the reductant for the NiO reduction, the corresponding mechanisms behind this process will be examined first.

The overall phase transformation sequence with increasing temper-

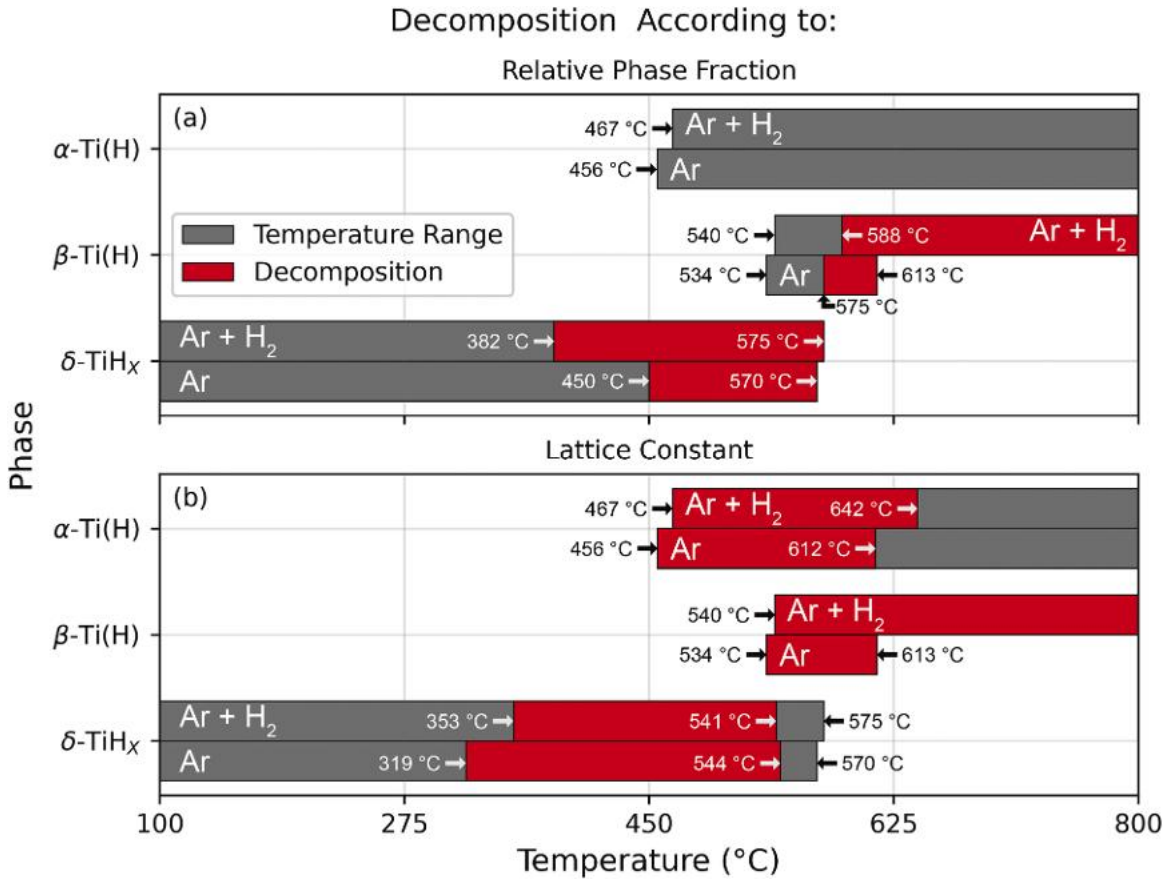

Fig. 9. Comparison of the temperature ranges, where phases are present, and the decomposition temperature range. (a) Temperature and decomposition range according to the relative phase fraction change extracted from Fig. 5. (b) Temperature and decomposition range according to the lattice constant extracted from Fig. 6.

ature ($\delta \rightarrow \delta + \alpha \rightarrow \delta + \alpha + \beta \rightarrow \alpha + \beta \rightarrow \alpha$) during hydride decomposition remains consistent regardless of the atmosphere and aligns with the report of Jiménez et al. [48]. The onset temperature of thermal decomposition, however, reveals a slight difference compared to the literature (Fig. 9). In general, the onset temperature of each transformation step appears consistently lower than in the case of Jiménez et al. [48], which might be explained by the presence of Ni/NiO or different flow rates of Ar during the experiments. Based on the relative phase fractions obtained from the SXRD data, the phase transformation sequence in the Ar and Ar + 5% H_2 cases are summarized as Eq. (4.1) and (4.2), respectively. In both cases, the appearance of the α-Ti(H) is observed at ~460 °C, prior to the occurrence of the β-Ti(H) phase (~537 °C in both cases). This contradicts the expected phase transformation sequence ($\delta \rightarrow \delta + \beta$) according to the Ti-H diagram **(Supplementary Fig. S4)**, where, based on the hydrogen content, the β-Ti(H) phase should form first. Jiménez et al. [48] rationalized this process with a core-shell model of the hydride decomposition, which also explains the simultaneous presence of δ, β-Ti(H), and α-Ti(H) (534 °C to 575 °C), when the hydride decomposition progresses. This finding is also validated based on the findings of the present study. At ~573 °C, the δ core is fully converted into the β-phase in both cases. The final conversion step is the decomposition of β-Ti(H) to α-Ti(H). Here, however, the most significant difference between both cases is observed. As hydrogen is a β stabilizer, the β-Ti(H) phase is stabilized up to 800 °C even when small amounts of H_2 are present in the atmosphere, compared to pure Ar (613 °C). In general, the hydrogen release (from δ-TiH_x, β-Ti(H), and α-Ti(H)) is delayed towards higher temperatures, as the equilibrium is shifted towards the hydrides, when hydrogen is present in the atmosphere. The shift of inception and decomposition complete temperatures of the α-Ti(H) and δ phases, however, are too small to show a significant change in decomposition behavior.

$$\delta \xrightarrow{456\ ^\circ C} \delta + \alpha \xrightarrow{534\ ^\circ C} \delta + \alpha + \beta \xrightarrow{575\ ^\circ C} \alpha + \beta \xrightarrow{613\ ^\circ C} \alpha \quad (4.1)$$

$$\delta \xrightarrow{467\ ^\circ C} \delta + \alpha \xrightarrow{540\ ^\circ C} \delta + \alpha + \beta \xrightarrow{570\ ^\circ C} \alpha + \beta \xrightarrow{\sim 800\ ^\circ C} \alpha \quad (4.2)$$

Resorting back to the overall synthesis kinetics (Fig. 2), a few discrepancies are observed when compared with the SXRD results, motivating more dedicated mechanistic rationalization. As evidenced in the TGA measurements, the first convoluted peak is present at ~370 °C under an Ar atmosphere, significantly lower than the δ-phase decomposition inception temperature indicated by SXRD. Such a difference is likely due to the nonstoichiometric nature of the δ-phase, which allows for hydrogen release yet does not alter the relative phase fraction. The onset temperatures of δ-decomposition (Fig. 9) in Ar according to relative phase fraction change (~450 °C), lattice constant change (319 °C), and TGA conversion rate peak (370 °C T_{p1} Fig. 2(b)), deviate significantly. As previously mentioned, it is possible for hydrogen to be released from the δ, β-Ti(H), and α-Ti(H) phase without a change in relative phase fraction due to the non-stoichiometric nature of those phases. As such, the lattice parameter becomes a more precise indicator of phase decomposition, when the lattice contracts as hydrogen is leaving the interstitial sites. This observation is also supported by the better correlation between lattice-based decomposition of the δ-phase and the onset of reduction according to the TGA measurement in Ar, compared to the relative phase fraction-based determination of decomposition start temperature. This also applies to the α-Ti(H) phase as well, here the c/a ratio is considered. With this in mind, the convoluted double peak ($T_{p1} = 370$ °C, $T_{p2} = 463$ °C) of the TGA measurement for Ar corresponds with the start of the δ and α decomposition (319 °C, 456 °C) respectively.

When 5% H_2 is present in the atmosphere, the two characteristic peaks of the TGA measurement are deconvoluted. Especially, T_{p1} (Fig. 2 (b)) shifts towards a lower temperature (276 °C). As suggested by the lattice constant evolution of the δ-phase, its decomposition begins at 353 °C. However, since the conversion rate has already decreased down to zero at ~340 °C, the majority of the sample mass loss corresponding to NiO reduction is driven by the H_2 present in the atmosphere. The NiO reduction will be discussed in detail in Section 4.1.2. Due to the NiO reduction *via* the atmospheric 5% H_2, the relative δ-phase fraction appears to be increasing (Fig. 5(b1)). However, since the phase fraction is relative to the sample mass and the δ-phase remains unchanged, the mass percentage of δ-TiH_x has to increase when the sample mass is decreasing due to reduction. The second peak (T_{p2} Fig. 2(b)) at 463 °C correlates to the alpha phase formation. According to San-Martin and Manchester [47], the composition of the α-, β-, and δ-phases are 0–8.38 at.%, 0–60.32 at.% and 51.22–66.67 at.% H, *i.e.* the β-α transition corresponds to the highest hydrogen release; hence the TGA peaks corresponds to the inception of α-Ti(H), as a product of β-Ti(H) decomposition. Since the NiO reduction and hydride decomposition are directly linked in Ar, each hydrogen release results in a NiO reduction, increasing the signal intensity for the TGA, making δ- and β-decomposition visible.

Table 3
Overview of average hydride decomposition kinetics. Two values are given, one calculated from the relative phase fraction (Fig. 5) the other one based on the lattice constants (Fig. 6). Hence, the decomposition rate of α-Ti(H) can only be evaluated based on the c/a ratio.

Sample	Based on	δ	β	α
Ar	Rel. phase frac. (Rel.wt.%/ °C)	−0.31	−0.76	
	Lattice const. for δ, β: (nm/ °C)10^{-3} for α c/a: (1/ °C) 10^{-3}	−17.78	−88.61	−0.26
Ar + 5% H_2	Rel. phase frac. (Rel.wt.%/ °C)	−0.22	−0.09	
	Lattice const. for δ, β: (nm/ °C)10^{-3} for α c/a: (1/ °C) 10^{-3}	- 21.28	−26.92	−0.11

The kinetics of hydride decomposition are similar between pure Ar and Ar + 5% H_2. During δ decomposition, the relative phase fraction and lattice constant change rates are similar between both experimental conditions (Table 3). Whereas, according to the lattice constant analyses, the δ decomposition temperature appears to be higher when H_2 is present in the atmosphere. When the decomposition is activated, the decomposition rate (according to the lattice constant) is faster, likely due to the elevated temperatures, where diffusion is substantially accelerated, due to the underlying Arrhenius dependence.

Similar to the phase stability range, the β-Ti(H) decomposition rate is strongly influenced by the presence of H_2 in the atmosphere. The decomposition rate of β-Ti(H) based on the relative mass fraction is increased almost ten-fold and the decomposition rate based on the lattice parameter is almost doubled, indicating that hydrogen reacts as a β-Ti stabilizer and decreases the decomposition rate of β-Ti(H). Since the lattice constant of β-Ti(H) is linearly decreasing with temperature (Fig. 6 (b1)) and remaining constant during the isothermal holding period, while the relative phase fraction is decreasing monotonically, the hydrogen content is insufficient to reach equilibrium conditions for β-Ti(H). An alternative rationalization could be the selective oxidization of Ti (increasing oxide content **(Supplementary Fig. S6 (b))**, since O acts as α stabilizing and thus shifts the equilibrium towards α-Ti(H). The c/a ratio of α-Ti(H) decreases twice as fast in pure Ar compared to Ar + 5% H_2 (Fig. 6(c1)). This effect can be attributed to the smaller lattice constant observed in Ar, which is likely due to residual hydrogen solubility in α-Ti causing lattice expansion in the Ar + 5% H_2 atmosphere, as the decomposition temperature is similar. With increasing temperature, the c/a ratio is increasing in Ar, moving closer to Ar + 5% H_2. A plausible explanation for this behavior could be thermal expansion or interstitial oxygen, which merit future study.

4.1.2. Oxide reduction, local oxidation, and possible metallothermic reaction mechanisms

With metallic Ti emerging through the thermal decomposition of Ti-

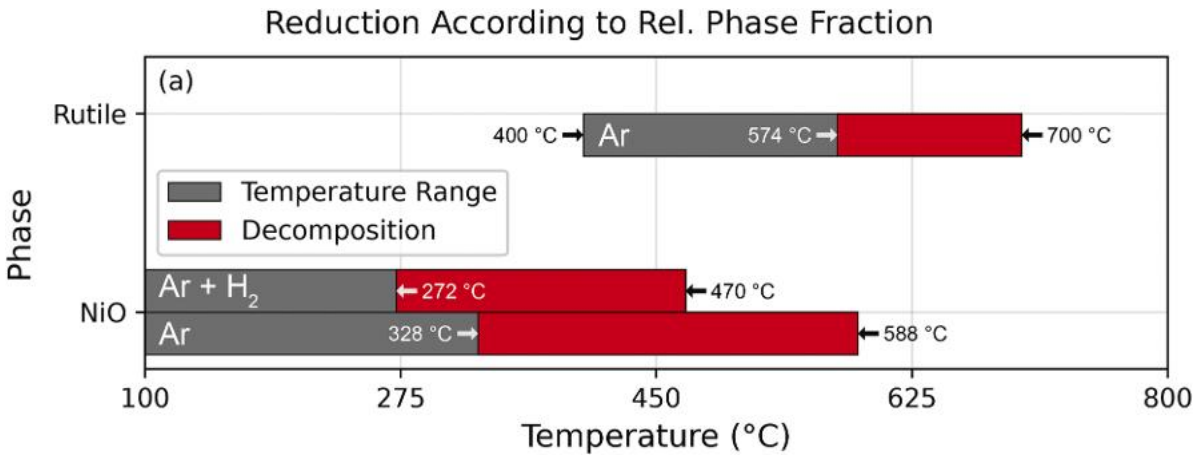

Fig. 10. Temperature ranges of oxides and the respective reduction temperatures. The temperature ranges were determined on the relative phase fraction of the oxide phases taken from Fig. 5.

hydrides, the second component required for solid state alloying is metallic Ni, of which the reduction pathways are discussed next.

As previously mentioned, the most noticeable distinction between the Ar and Ar + 5% H_2 samples is the temperature at which NiO starts to be reduced, since a change in relative phase fraction can be observed in Fig. 5. In pure Ar, NiO reduction occurs at ~328 °C, whereas in Ar + 5% H_2, the relative NiO phase fraction decreases at ~272 °C. This is in good agreement with the TGA measurements (Fig. 2), where the T_{p1} peaks occur at 370 and 276 °C, respectively. Because the reported reduction temperature of NiO in H_2 is 270 °C [50], the delayed reduction of NiO in pure Ar indicates the absence of a suitable reductant below 328 °C. Only with the decrease of the δ-lattice parameter at 319 °C, hydrogen from thermal decomposition becomes available for the reduction and NiO consequently is being reduced. When 5% hydrogen is present in the atmosphere, the relative phase fraction of NiO decreases at ~272 °C, aligning well with the literature [50]. As previously discussed, the reductant needed for this NiO reduction cannot originate from the δ-phase, as the temperature is too low for thermal decomposition. Since the only accessible reductant is the hydrogen in the atmosphere, the NiO has to be reduced by the 5% of H_2 pre-mixed in the atmosphere.

NiO is reduced more than twice as fast when hydrogen is present in the atmosphere compared to the pure Ar scenario (−0.45 at.%/ °C and −0.20 at.%/ °C respectively). Since the δ-phase is not decomposing while NiO is being reduced in Ar + 5% H_2, the reduction of NiO is rate limited either by the transport of hydrogen to NiO or the removal of H_2O from the sample. The decomposition rate of the δ-phase, based on the lattice constant change, in Ar and Ar + 5% H_2 (−0.22 at.%/ °C and −0.27 at.%/ °C respectively), however, remains similar in both cases. This clearly shows that the decomposition of the δ-phase and the reduction of NiO are coupled in pure Ar. Because of the elevated reduction temperature and a similar decomposition/reduction rate, it can be concluded that the hydride decomposition is the rate controlling step in pure Ar. The increased reduction rate in Ar + 5% H_2 however clearly shows that the NiO reduction is rate independent and therefore must rely on the atmospheric H_2 instead.

In addition to the hydrogen-based reduction, an alternative reduction pathway for NiO might be the metallothermic reduction with Ti [51]:

$$2NiO + Ti \rightarrow Ni + TiO_2$$

Padhan et al., however, estimated the temperature for a self-sustaining reduction reaction should be approaching 4000 K [51]. As the δ-phase decomposes to α-Ti(H), the formation of Rutile (Fig. 5 inset (a3)) is observed. This is in good agreement with the TGA results (Fig. 2 (a)), where the overall conversion degree does not exceed 70%. Since the oxygen does not leave the sample but is instead bound in the rutile phase, the conversion degree based on mass change will not increase, even though NiO will be fully reduced as seen in Fig. 5(a). Since Rutile and α-Ti(H) appear at lower temperatures compared to β-Ti(H), the rutile phase might be the oxidation product of α-Ti(H). Interestingly, as soon as the β-Ti(H) phase begins to decrease in its relative fraction, the rutile phase reveals a similar decreasing trend until no more rutile peak can be observed. Jiménez et al. [48] observed a similar behavior during the thermal decomposition of a peroxidized TiH_2 sample. They suggest the self-reduction of TiO_2 by α-Ti, at elevated temperatures (535 °C to 623 °C) as the solubility in α-Ti is increasing, leading to a more uniform distribution of oxygen throughout the sample. This in turn is also consistent with the decrease in reduction degree found for the Ar case in the TGA measurement. Overall, 33.78 at.% of NiO must have been reduced by metallic Ti, based on the assumptions that (1) all hydrogen has left the sample by 800 °C; (2) NiO has been fully reduced; and (3) Ti is the only active reductant in the solid state. Concluding the discussed reduction mechanisms, an overview can be found in Fig. 10.

4.1.3. *Intermetallic phase formation*

Through the previously described reactions, metallic Ti and Ni become available for the final mechanism of the conceived one-step process of solid-state reactive alloying of NiTi - the formation of intermetallic Ni-Ti phases by solid state diffusion.

It can be assumed that during decomposition and reduction the overall volumes of the initial NiO and TiH_2 particles are decreasing, nevertheless, the alloying process can be conceived as a Ni- and Ti-particle in contact with each other. Similar to a macroscopic diffusion couple, the concentration gradient between those two particles will drive solid state interdiffusion of Ni and Ti. At a given temperature, the diffusion couple can be represented by a horizontal line in the phase diagram **(Supplementary Fig. S11)**. With proceeding diffusion, all five stable phases (Ti, Ti_2Ni, NiTi, Ni_3Ti, Ni) are expected to form, as the stoichiometry of the intermetallic line compounds (Ti_2Ni, NiTi and Ni_3Ti) will be met by the concentration gradient between the two particles. This behavior has been observed in several cases in the literature for diffusion couples and for Ni-Ti powder mixtures [52–54].

Because the initial conditions (presence of Ni and Ti particles in contact to each other) after reduction and thermal decomposition are similar, it is not surprising that at elevated temperatures (650–700 °C) intermetallic phases (Ti_2Ni and Ni_3Ti) form in both atmospheres. The absence of the NiTi phase may be attributed to either inadequate contact between Ni and Ti particles, which limits diffusion, or an insufficient holding time at 800 °C to allow NiTi phase formation *via* diffusion.

In pure Ar, the growth of Ti_2Ni and Ni_3Ti shows asymptotic behavior (Fig. 5) and cumulates in an overall relative phase fraction of 24% and 17% after isothermal holding. In Ar + 5% H_2 a similar asymptotic

Table 4
Rate of relative phase fraction change during heating of both samples.

Sample	Ni	α-Ti(H)	β-Ti(H)	Ti_2Ni	Ni_3Ti
Ar (Rel.wt.%/ °C)	−0.07	−0.08	-	0.08	0.04
Ar + 5% H_2 (Rel.wt.%/ °C)	−0.03	0.06	−0.08	0.04	0.02

Table 5
Rate of relative phase fraction change during isothermal holding of both samples.

Sample	Ni	α-Ti(H)	β-Ti(H)	Ti_2Ni	Ni_3Ti
Ar (Rel.wt.%/min)	−0.14	−0.11	-	0.12	0.13
Ar + 5% H_2 (Rel.wt.%/min)	−0.04	0.04	−0.17	0.05	0.016

behavior is observed, the resulting relative phase fractions of Ti_2Ni and Ni_3Ti however significantly decrease (9% and 2% respectively). As the microstructure in both samples is similar, the difference in intermetallic phase fraction might be solely ascribed to the presence of H_2 in the atmosphere. As the intermetallic phases form, Ni-, α- and β-Ti(H)-phases should be consumed, thus the respective relative phase fractions will decrease. This remains consistent for the Ar case, where the Ni (57% to 33%) and α-Ti(H) (38% to 17%) relative phase fractions decrease. In case of Ar + 5% H_2, the relative weight fraction of Ni is decreasing (55% to 47%), the α-Ti(H) phase however is increasing (3% to 20%). This can be explained by the decomposition of β-Ti(H), serving as an additional Ti-source, for Ti_2Ni-, Ni_3Ti- and α-Ti(H)-phase formation.

The average phase fraction change rate has been calculated during heating and isothermal holding (Tables 4 and 5). As the system is not mass conserving, detailed quantitative analysis and comparison between the individual phases is not advised. Instead, a more general semi-quantitative interpretation will be discussed next. In pure Ar, Ni and α-Ti (H) are consumed at a similar rate, as Ti_2Ni and Ni_3Ti are present, indicating that almost all Ni and Ti are converted to Ti_2Ni and Ni_3Ti

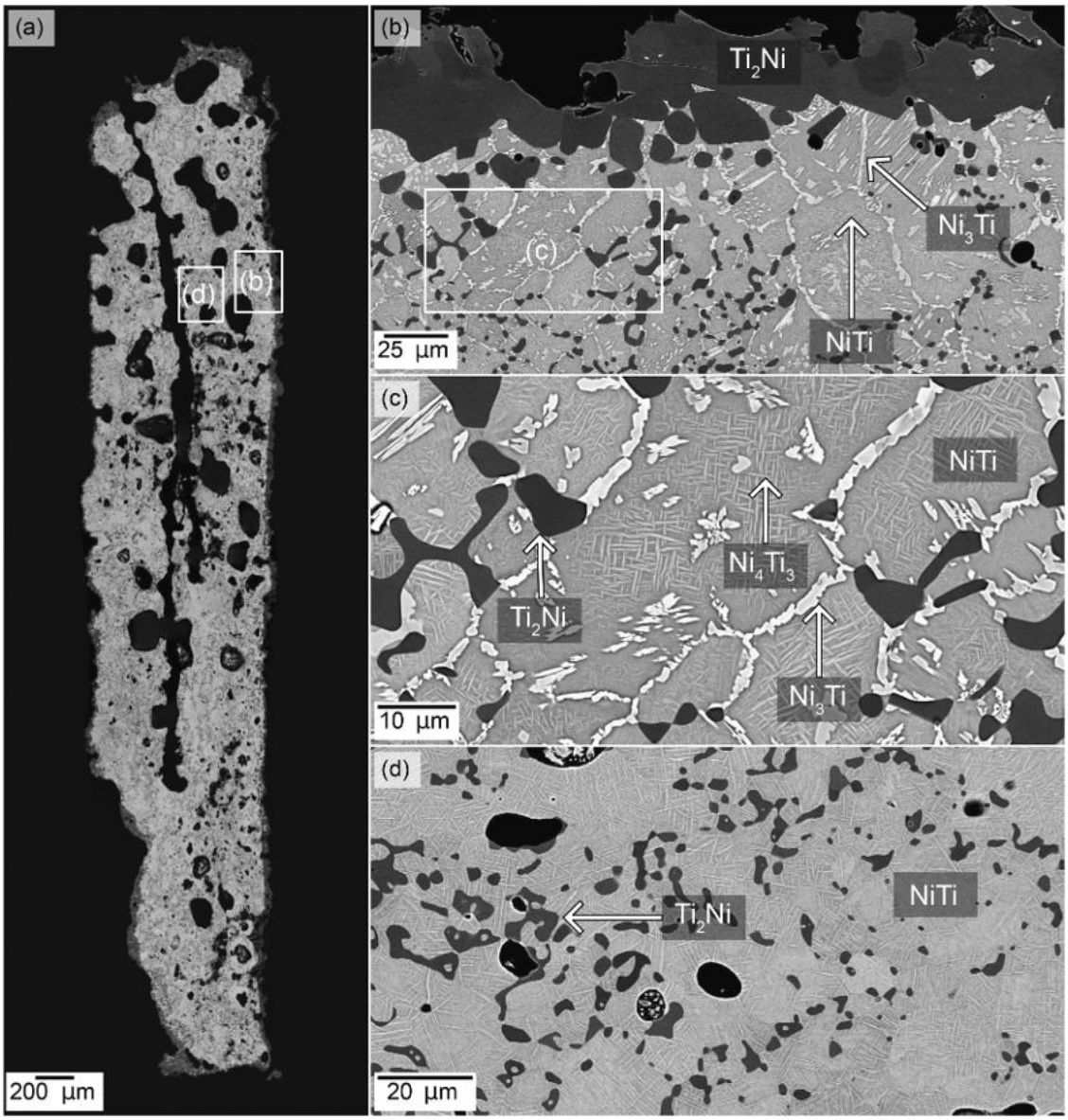

Fig. 11. Microstructure of the sample in the validation experiment. (a) Sample overview. Positions of higher magnification micrographs are marked. (b-c) Microstructure of the sample rim. The sample is surrounded by a dark Ti_2Ni shell, due to oxidization. The depletion zone below the Ti_2Ni layer forms Ni-rich Ni_3Ti and Ni_4Ti_3 precipitates. The uniform gray matrix is the NiTi phase. (d) In the sample bulk, the amount of Ti_2Ni is decreased. The NiTi content is increased, Ni_3Ti is not present. Inside the NiTi phase, needle shaped Ni_4Ti_3 is observed.

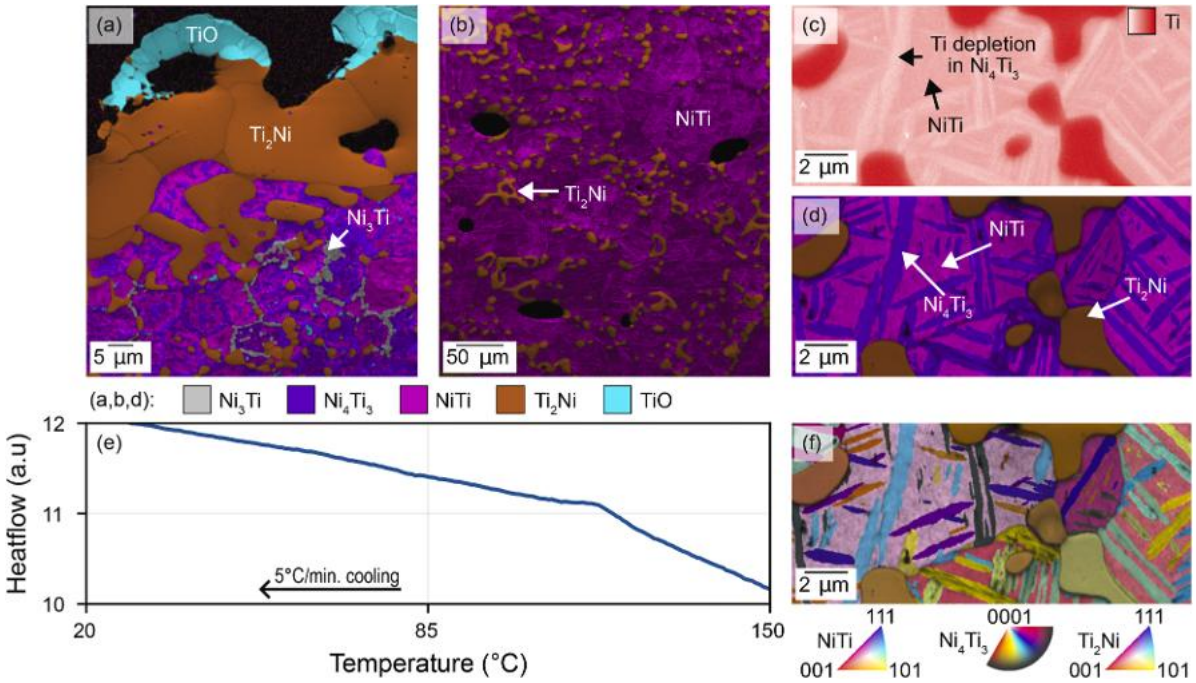

Fig. 12. EBSD, EDS and DSC analyses for validation. (a) Measurement of the sample rim. In addition to the Ti_2Ni layer on the outside characterized by EDS (Fig. 11) a TiO layer is clearly visible. Due to Ti depletion underneath the Ti_2Ni layer, Ni_3Ti and Ni_4Ti_3 precipitates form at the grain boundaries and in the NiTi crystals, respectively. Due to the fine topology and dispersion of the Ni_4Ti_3 precipitates, making a clear distinction challenging at this magnification, a detailed EDS and EBSD analysis is done in (c) and (d). (b) In the sample center, the influence of the Ti depletion zone is less pronounced. Ti_2Ni, and NiTi can be characterized at this magnification and yield a NiTi/Ni_4Ti_3 phase fraction of 82.2%. Due to resolution limitations, NiTi and Ni_4Ti_3 are characterized as NiTi. (c) To confirm the Ni_4Ti_3 phase in needle morphology, an EDS map of a smaller area has been taken. The Ti content clearly is decreased in the needles compared to the NiTi matrix. (d, f) Further EBSD analysisA of (c) confirms the Ni_4Ti_3 crystal structure. (e) DSC measurement of the validation sample, no clear phase transformation peaks.

during heating and isothermal holding. While the consumption rate of Ni and β-Ti(H) still correlates well with the formation rates of Ti_2Ni and Ni_3Ti, during the isothermal holding the formation of α-Ti(H), Ti_2Ni and Ni_3Ti is almost stagnant, despite the pronounced decomposition of β-Ti (H). As the Ti consumption does not match the intermetallic formation, the only plausible explanation is the formation of Ti-O phases. This hypothesis is confirmed in **(Supplementary Fig. S6)**, where at ~588 °C, the TiO phase starts to form. During isothermal holding, the amount of relative phase fractions of rutile and TiO increase. This also matches with the microstructure (Fig. 8(a, c)), where the sample rim shows a different microstructure compared to the sample bulk, indicating a reaction of the sample surface with the atmosphere. Compared to the Ar case, the overall amount of TiO and rutile is higher when 5% of H_2 is present in the atmosphere. This phenomenon appears at first view counterintuitive, as it is expected that the oxygen partial pressure in the atmosphere should be reduced when H_2 is present. One possible explanation for this might be the increased relative phase fraction of Ni-Ti intermetallic phases in the pure Ar sample. As seen in Fig. 7(b), the Ti-particle forms a shell of Ni-Ti intermetallic phases. Ni-Ti intermetallic phases in turn are less prone to oxidation and protect the unalloyed Ti from oxidation, as can be seen by the overall lower oxygen content according to the EDS-measurement and the overall lower relative phase fraction of TiO and rutile according to SXRD. An explanation for the decreased oxygen affinity of Ti-alloys was given by Sekimoto et al. in the form of a decrease of Ti-activity when alloyed [55].

There are two potential factors influencing the formation of Ti_2Ni and Ni_3Ti, namely, the presence of hydrogen and oxygen. As the Ti_2Ni and Ti_4Ni_2O phases are isostructural [56], there will be no distinction between these two phases from SXRD results. The observed increasing fraction of the Ti_2Ni phase can also be ascribed to the formation of the Ti_4Ni_2O phase. Compared to the initial 50 at.% mixture, the Ti_2Ni phase is enriched in Ti, which in turn entails a Ti depletion range in the surrounding area, benefiting the formation of Ni_3Ti. As discussed in the previous section, ~1/3 of the initial NiO is reduced by Ti through a metallothermic reaction, when the atmosphere is pure Ar. With the oxygen presenting in solid solution, the formation of Ti_2Ni/Ti_4Ni_2O might be facilitated. From the resulting Ti depletion, the Ni_3Ti formation will be enhanced as well. The resulting Ni-Ti intermetallic shell will protect the sample from further atmospheric oxidization, due to the reduced Ti activity, when alloyed [55].

When 5% H_2 is present in the atmosphere, the overall reduction degree increases initially, as the majority of NiO is reduced by H_2, decreasing the interstitial O and therefore hindering the formation of Ti_2Ni/Ti_4Ni_2O and Ni_3Ti. During extended isothermal holding, the unprotected Ti is oxidized, leading to the overall increase of oxygen content. An alternative explanation might be the passivation of Ti when hydrogen is present, as the solid-state alloying occurs only when fully decomposed α-Ti is present, *i.e.* the solid-state alloying is activated at higher temperatures in 5% H_2. To distinguish between the two discussed mechanisms, an experiment with Ni and TiH_2 might be advised in future study.

In the context of these mechanisms, the introduction of O *via* NiO might be beneficial for the formation of the NiTi phase, as it will be formed from Ni_3Ti and Ti_2Ni [54]. Difficulties however might arise, from the fact that Ti_4Ni_2O is stabilized by O, changing the amount of Ti available for NiTi alloying. The benefit of initial reduced oxygen content with increased oxidization resistance due to intermetallic formation might be combined, by mixing H_2 in the atmosphere and increasing the holding temperature, which would increase the diffusion kinetics supporting intermetallic formation and oxidization suppression.

Concluding the foregoing discussion, successful synthesis of the desired NiTi might be achieved based on the following mechanistic guidelines:

(1) The addition of hydrogen to the atmosphere will decrease the O content of the sample, facilitating the formation of NiTi.

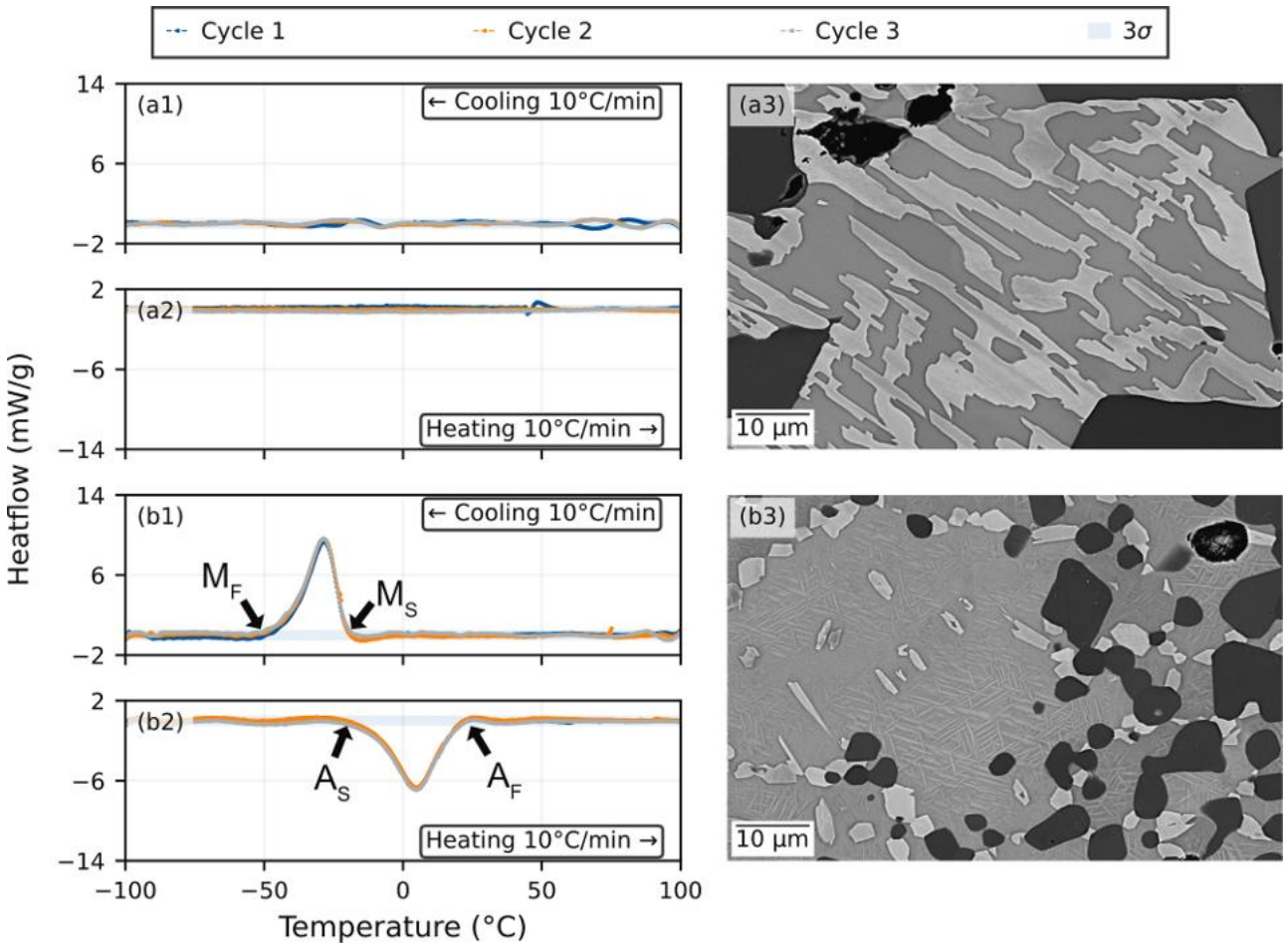

Fig. 13. DSC results after quenching (a) and dehydrogenation (b). (a) To mitigate excessive oxidization and high Ni_4Ti_3 content a bigger sample (500 mg) was processed at 1150 °C. Additionally, the sample was annealed at 900 °C for 1 h under a protective Ar atmosphere and was subsequently quenched in water, resulting in a reduction of Ni_4Ti_3 phase (a3). (b) The dehydrogenated sample has an increased Ni_4Ti_3 content (b3) and shows pronounced phase transformation behavior.

(2) Increasing the isothermal holding temperature will increase the diffusion rate, and reduce the overall process time, which in turn helps to minimize surface oxidization.
(3) The introduction of hydrogen will delay the hydride decomposition to higher temperatures, minimizing the time Ti is exposed to retained atmospheric oxygen.

4.2. *Validation of the synthesis guidelines*

With the proposed guidelines established in the foregoing section, a validation synthesis experiment was next performed adopting the consistent parameters of Section 2, yet with a higher isothermal holding temperature of 1150 °C, intended to facilitate solid-state alloying. As discussed earlier, 5% H_2 is introduced to prevent the metallothermic reduction of NiO and decrease the amount of initial oxygen in the sample. As can be seen from the micrographs (Fig. 11) the density of the sample increases compared to both samples processed at 800 °C, a sign of increased diffusion and consolidation. The entire sample is covered by a darker region, which, based on EDS and EBSD analysis, consists of Ti_2Ni/Ti_4Ni_2O and TiO phases (Figs. 11 and 12). This is in good agreement with the previous discussion, the oxygen partial pressure of the atmosphere leads to the formation of TiO and stabilizes the Ti_2Ni/Ti_4Ni_2O phase.

As Ti_2Ni/Ti_4Ni_2O is enriched in Ti compared to the global nominal composition (50 at.% Ti), a Ti-depleted region is expected and indeed forms underneath the oxidized sample shell where Ni-rich Ni_3Ti precipitates nucleate at the grain boundaries of NiTi, counterbalancing the local Ti loss. In addition, needle-like metastable Ni_4Ti_3 precipitates form in the NiTi grain interior, as confirmed by EDS and EBSD measurements. A less pronounced microstructural influence of the Ti depleted zone is present at the sample center (Fig. 12(b)), where NiTi and Ni_4Ti_3 constitutes the major phases (82.2%) accompanied by a minor amount of the Ti_2Ni phase (15.7%). Higher magnification SEM-EBSD analyses (Fig. 12 (c, d, f)) further reveal that the fractions of the NiTi and the Ni_4Ti_3 phases achieve 41.0% and 42.4%, respectively. Based on these findings, the overall NiTi content in the sample center reaches 33.7%.

Even though the NiTi phase fraction is significant, no distinct peaks were observed (Fig. 12(e)). According to literature, the phase transformation temperature depends on the Ni content in the NiTi phase and can shift between 66 and −62 °C (M_S) [57]. One possible reason for the absence of the characteristic phase transformation, is the high phase fraction of Ni_4Ti_3 precipitates, which constrain the martensitic transformation of the NiTi matrix, resulting in incomplete phase transition.

To mitigate the effects of the Ni_4Ti_3 content on the phase transformation behavior, a second sample was prepared along with the identical process, however, the sample size was in this case increased to 500 mg to reduce surface-to-volume ratio. An addition annealing step was performed at 900 °C for 1 h under a protective Ar atmosphere. After a baseline subtraction from the raw DSC data, no exo- and endothermic peaks were observed during the heating and cooling cycles of the sample (Fig. 13(a1–2)). Since the microstructure does not show a significant amount of the needle like Ni_4Ti_3 phase (Fig. 13(a3)), the previous hypothesis of a constrained Ni_4Ti_3 phase is insufficient to rationalize the current observations.

Table 6
Measured DSC transformation Temperatures.

Cycle	A_S (°C)	A_F (°C)	M_S (°C)	M_F (°C)
1	−11,31	18.58	−20.47	−41.90
2	−11.22	18.40	−20.31	−41.95
3	−12.29	18.30	−20.40	−42.35

M. Kuběnová et al. [58] describe the suppression of the martensitic transformation by the presence of interstitial H. To determine the influence of H on the phase transformation behavior of the sample, the previously annealed and quenched sample was dehydrogenated in vacuum at 900 °C for 2 h. After the dehydrogenation treatment an additional DSC measurement was conducted (Fig. 13(b1–2)), revealing clear endo- and exothermic peaks during heating and cooling of the sample. The measured A_S,A_F,M_S and M_F temperatures (Table 6) all correspond well with literature [57,37], showcasing the importance of controlling interstitial hydrogen for the desired austenitic- martensitic phase transformation. By effectively annealing the sample in vacuum at 900 °C the effects of quenching were mostly reverted, with the characteristic needle like Ni_4Ti_3 structure visible again (Fig. 13(b3)). This means that it can be concluded that interstitial hydrogen plays a more significant role for the phase transformation behavior than the Ni_4Ti_3 phase fraction.

Based on the previous microstructure analysis, we conclude that the proposed synthesis pathways and boundary condition guidelines indeed lead to the formation of a significant quantity (NiTi/Ni_4Ti_3 phase fraction of 82.2% in the sample center) of the desired NiTi phase. Interstitial hydrogen tends to hinder the austenite-martensite transformation potency of the NiTi phase that can potentially enable shape memory effect. A dehydrogenation step in vacuum enables the characteristic austenitic martensitic phase transformation. Further fine-tuning of the initial composition to account for the Ti loss due to oxidation might suppress the formation of the Ni_4Ti_3 phase. Alternatively, annealing and subsequent quenching are also advised in future synthesis to minimize the Ni_4Ti_3 phase fraction.

4.3. Mechanistic summary and insights into sustainable solid-state reactive alloy making

In this section, the previously discussed mechanisms during reactive solid-state alloying, are summarized and presented in a schematic protocol for a NiO and Ti-hydride particle (Fig. 14). When 5% H_2 is present in the atmosphere (Fig. 14(b)), NiO is reduced as soon as the reduction temperature is reached. In pure Ar (Fig. 14(a)), the reductant becomes only accessible when the thermal decomposition of Ti-hydride incepts at elevated temperatures compared to the Ar + 5% H_2 atmosphere. Following a core-shell model, the NiO and δ-TiH_x particle reduce and decompose from the outside towards the particle core. The δ-TiH_x

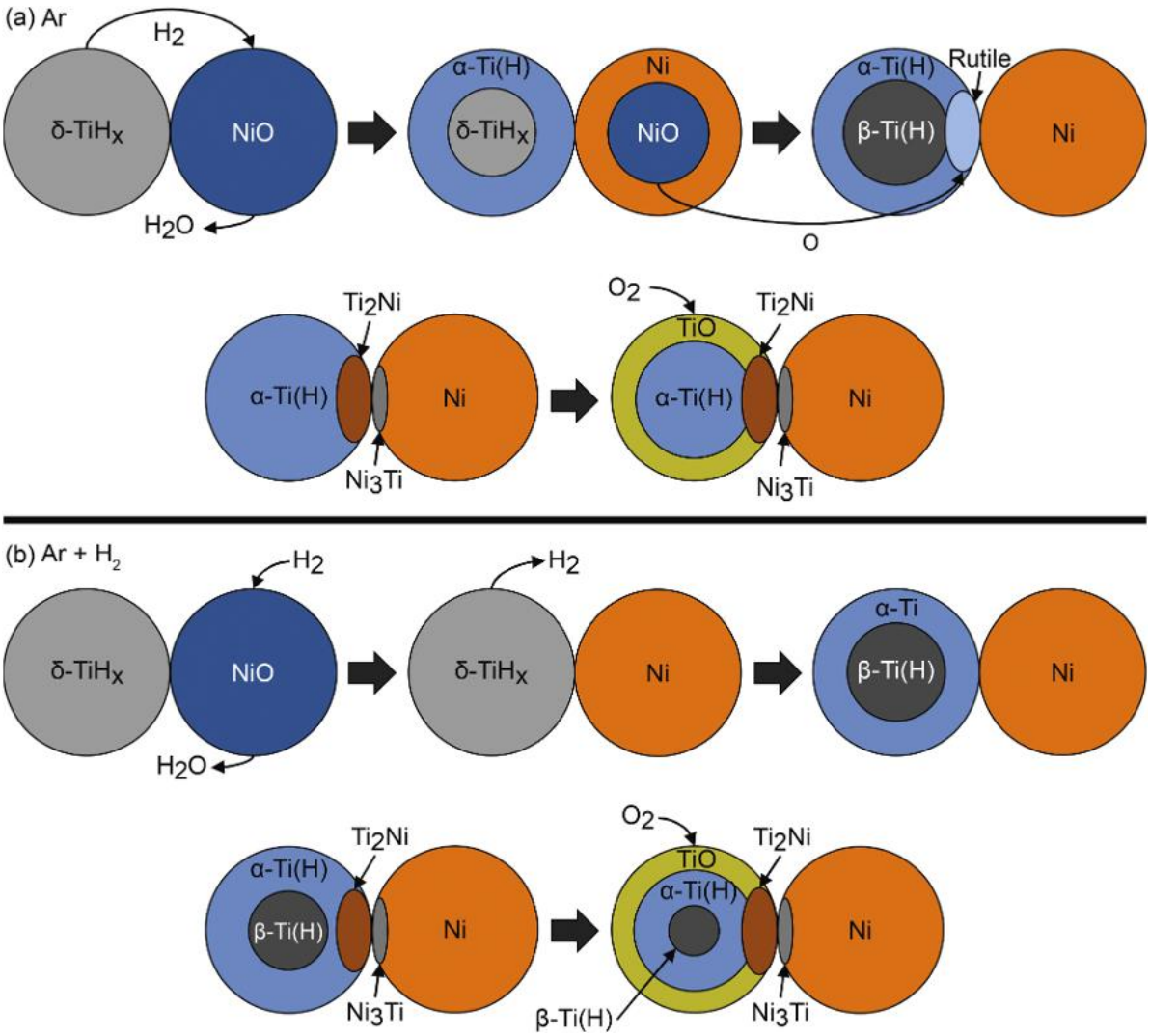

Fig. 14. Schematic overview of the reactive solid-state alloy making. (a) Schematic overview in pure Ar. (b) Schematic overview in Ar + 5% of H_2.

decomposition follows the same sequence in both cases ($\delta \rightarrow \delta + \alpha \rightarrow \delta + \alpha + \beta \rightarrow \alpha + \beta \rightarrow \alpha$). As NiO and α- or β-Ti(H) are in contact, signs of a metallothermic reduction are observed ($Ti + 2NiO = TiO_2 + 2Ni$) in pure Ar atmosphere, resulting in Rutile formation. With increasing temperature and overall amount of α-Ti(H), the amount of rutile is decreasing, which can be explained by the self-reduction of Ti. When Ni and Ti diffusion is thermally activated and the flux is sufficient, solid-state alloying is present in both cases. Driven by the concentration gradient, the intermetallic phases Ti_2Ni and Ni_3Ti form. As confirmed by the validation experiment, with a sufficiently high temperature, the diffusion rate is sufficient to form NiTi in between the two intermetallic phases. During the process, small quantities of oxygen enter the reaction chamber. Hence, signs of surface oxidization, in the form of an TiO and Ti_4Ni_2O/Ti_2Ni layer, are also observed, leading to the formation of a Ti depletion region where Ni-rich Ni_3Ti and Ni_4Ti_3 precipitates form. Increasing the heating rate to 50 °C/min does not have a significant influence on the phase sequence **(Supplementary Fig. S8, Supplementary Fig. S10)**, however since reduction and decomposition of NiO and TiH_2 are thermally activated processes, increasing the heating rate will shift the onset of those mechanisms towards higher temperatures.

5. Conclusion

The concurrent reduction and alloying behavior of NiO-TiH_2 powder blends with a nominal composition of 50 at.% was investigated both in pure Ar and Ar + H_2 atmosphere at 800 °C, resulting in a conversion degree of 70% and 92%, respectively, into a mix of intermetallic products including Ti_2Ni/Ti_4Ni_2O, Ni_3Ti, Ni_4Ti_3, and NiTi. Through *in situ* SXRD, the phase transformation sequence of both cases was investigated and the major conclusions are summarized as follows:

(1) Hydride decomposition follows the sequence δ-TiH_x → α-Ti(H) → β-Ti(H) and completes around 613 °C and 800 °C for Ar and Ar + 5% H_2 respectively. In Ar + H_2, NiO reduction begins before hydride decomposition and finishes at 470 °C, whereas in pure Ar, hydride decomposition must supply hydrogen, causing NiO reduction and hydride breakdown to proceed simultaneously, finishing at 588 °C. A Ti-driven metallothermic reduction of NiO and transient rutile formation is also observed in pure Ar.
(2) After the NiO reduction and δ-TiH_x decomposition is completed, alloying of Ni and Ti *via* diffusion begins. The emergence of Ni–Ti intermetallic phases (Ti_2Ni, Ni_3Ti) strongly depends on the atmosphere condition. In Ar+H_2, the intermetallic formation is suppressed. This is most likely due to the reduced initial oxygen contamination, as there is no metallothermic NiO reduction, and the stabilization of β-Ti(H) by atmospheric hydrogen, reducing reactivity with atmospheric oxygen.
(3) Three major process design guidelines are recognized: first, introducing hydrogen to the atmosphere prevents metallothermic reduction of NiO; second, higher isothermal holding temperatures accelerate diffusion, thus mitigating oxidization; and third, hydrogen addition shifts hydride decomposition to higher temperatures, limiting Ti exposure to residual oxygen.

Based on the findings of the present study, it might be possible to reduce the amount of undesired intermetallic phases (Ti_2Ni, Ni_3Ti, and Ni_4Ti_3) by optimizing the temperature profile and the gas atmosphere to further limit oxygen contamination, supress interstitial hydrogen uptake, and mitigate the precipitation of Ni-rich phases.

CRediT authorship contribution statement

Lennart Hitzemann: Conceptualization, Investigation, Formal analysis, Visualization, Writing – original draft. **Shao Lou Wei:** Conceptualization, Investigation, Validation, Supervision, Writing – original draft, Writing – review & editing. **Stefan Zaefferer:** Investigation, Validation, Writing – review & editing. **Dierk Raabe:** Conceptualization, Validation, Supervision, Resources, Funding acquisition, Project administration, Writing – review & editing.

Declaration of competing interest

The authors declare the following financial interests/personal relationships which may be considered as potential competing interests:

Lennart Hitzemann, Shaolou Wei, Stefan Zaefferer, and Dierk Raabe Max Planck Institute for Sustainable Materials, 40237 Düsseldorf, Germany.

Acknowledgements

We acknowledge DESY (Hamburg, Germany), a member of the Helmholtz Association HGF, for the provision of experimental facilities. Parts of this research were carried out at PETRA III, beamline P21.1 [59]. We would like to thank Dr. Jiatu Liu for the assistance during the experiments. Beamtime was allocated for proposals I-20240761, I-20240759 and I-20251005.

D.R. acknowledges funding by the European Union, through the project ROC, sponsored by the European Research Council (ERC, grant number. 101054368).

S.L.W. acknowledges financial support from the MPG Scholarship and Alexander von Humboldt Research Fellowship (hosted by D.R.). S.L.W. and D.R. acknowledge the MPG-FhG Cooperation Grant MaRS. The authors also thank Dr. Frank Stein for useful technical exchanges.

Supplementary materials

Supplementary material associated with this article can be found, in the online version, at doi:10.1016/j.actamat.2026.122337.

References

[1] L. Chen, G. Msigwa, M. Yang, A.I. Osman, S. Fawzy, D.W. Rooney, P.-S. Yap, Strategies to achieve a carbon neutral society: a review, Environ. Chem. Lett. 20 (2022) 2277–2310, https://doi.org/10.1007/s10311-022-01435-8.
[2] S.L. Wei, Y. Ma, D. Raabe, One step from oxides to sustainable bulk alloys, Nature 633 (2024) 816–822, https://doi.org/10.1038/s41586-024-07932-w.
[3] X. Knigge, J. Radnik, Advanced materials for the energy transition. https://openumwelt.de/handle/123456789/10841, 2025 (accessed November 24, 2025).
[4] T. Koljonen, A. Lehtilä, K. Kiviranta, K. Koponen, L. Similä, Modelling of demands of selected minerals and metals in clean energy transition with 1.5–2.0 °C mitigation targets, in: M. Labriet, K. Espegren, G. Giannakidis, B.Ó Gallachóir (Eds.), Aligning the Energy Transition with the Sustainable Development Goals Key Insights from Energy System Modelling, Springer Nature Switzerland, Cham, 2024, pp. 225–245, https://doi.org/10.1007/978-3-031-58897-6_10.
[5] The energy transition is also driving a materials transition, World Econ. Forum (2024). https://www.weforum.org/stories/2024/08/the-energy-transition-is-creating-a-historic-materials-transition-heres-why/ (accessed November 24, 2025).
[6] European Commission, Directorate General for Internal Market, Industry, Entrepreneurship and SMEs., Study on the EU's List of Critical Raw Materials (2020): Critical Raw Materials Factsheets, Publications Office, LU, 2020. https://data.europa.eu/doi/10.2873/92480 (accessed November 24, 2025).
[7] European Commission, Directorate General for Internal Market, Industry, Entrepreneurship and SMEs., Study on the EU's List of Critical Raw Materials (2020): Final Report, Publications Office, LU, 2020. https://data.europa.eu/doi/10.2873/11619 (accessed November 24, 2025).
[8] V. Petrova, Metals in the circular economy, in: SHS Web Conference 120, 2021 02014, https://doi.org/10.1051/shsconf/202112002014.
[9] D. Raabe, The materials science behind sustainable metals and alloys, Chem. Rev. 123 (2023) 2436–2608, https://doi.org/10.1021/acs.chemrev.2c00799.
[10] L. Gast, J.M. Allwood, What bulk material production is possible on a transition to net zero emissions by 2050 with limited zero emissions resources? J. Clean. Prod. 423 (2023) 138346 https://doi.org/10.1016/j.jclepro.2023.138346.
[11] E. Van der Voet, L. Van Oers, M. Verboon, K. Kuipers, Environmental implications of future demand scenarios for metals: methodology and application to the case of seven major metals, J. Ind. Ecol. 23 (2019) 141–155, https://doi.org/10.1111/jiec.12722.
[12] R. Soni, R. Verma, R.K. Garg, V. Sharma, A critical review of recent advances in the aerospace materials, Mater. Today Proc. 113 (2024) 180–184, https://doi.org/10.1016/j.matpr.2023.08.108.
[13] J.W. Mwangi, L.T. Nguyen, V.D. Bui, T. Berger, H. Zeidler, A. Schubert, Nitinol manufacturing and micromachining: a review of processes and their suitability in

processing medical-grade nitinol, J. Manuf. Process. 38 (2019) 355–369, https://doi.org/10.1016/j.jmapro.2019.01.003.
[14] Z. Liu, L. Zhang, C. Fu, C. Zeng, X. Wu, W. Li, X. Ma, Structural, mechanical, and thermodynamic properties of Ni–Ti intermetallic compounds: first-principle calculation, J. Appl. Phys. 134 (2023) 085107, https://doi.org/10.1063/5.0159431.
[15] P.C. Priarone, G. Ingarao, R. di Lorenzo, L. Settineri, Influence of material-related aspects of additive and subtractive Ti-6Al-4V manufacturing on energy demand and carbon dioxide emissions, J. Ind. Ecol. 21 (2017) S191–S202, https://doi.org/10.1111/jiec.12523.
[16] Nachhaltigkeit | ELG Deutschland, (n.d.). https://www.elgmetals.com/de-de/nachhaltigkeit/(accessed October 31, 2025).
[17] R. Kocich, I. Szurman, M. Kursa, R. Kocich, I. Szurman, M. Kursa, The methods of preparation of Ti-Ni-X alloys and their forming. Shape Memory Alloys - Processing Characterization and Applications, IntechOpen, 2013, https://doi.org/10.5772/50067.
[18] A.R. Pelton, S.M. Russell, J. DiCello, The physical metallurgy of nitinol for medical applications, JOM 55 (2003) 33–37, https://doi.org/10.1007/s11837-003-0243-3.
[19] K. Otsuka, X. Ren, Physical metallurgy of Ti–Ni-based shape memory alloys, Prog. Mater. Sci. 50 (2005) 511–678, https://doi.org/10.1016/j.pmatsci.2004.10.001.
[20] S.K. Patel, B. Swain, R. Roshan, N.K. Sahu, A. Behera, A brief review of shape memory effects and fabrication processes of NiTi shape memory alloys, Mater, Today Proc. 33 (2020) 5552–5556, https://doi.org/10.1016/j.matpr.2020.03.539.
[21] S.L. Wei, D. Raabe, Superelastic titanium alloy has potential for space missions, Nature 638 (2025) 896–897, https://doi.org/10.1038/d41586-025-00301-1.
[22] M.H. Wu, Fabrication of nitinol materials and components, Mater. Sci. Forum 394-395 (2002) 285–292, https://doi.org/10.4028/www.scientific.net/MSF.394-395.285.
[23] J. Mentz, J. Frenzel, M.F.-X. Wagner, K. Neuking, G. Eggeler, H.P. Buchkremer, D. Stöver, Powder metallurgical processing of NiTi shape memory alloys with elevated transformation temperatures, Mater. Sci. Eng. A 491 (2008) 270–278, https://doi.org/10.1016/j.msea.2008.01.084.
[24] B. Bertheville, J.-E. Bidaux, Enhanced powder sintering of near-equiatomic NiTi shape-memory alloys using *Ca* reductant vapor, J. Alloys Compd. 387 (2005) 211–216, https://doi.org/10.1016/j.jallcom.2004.06.079.
[25] B.-Y. Li, L.-J. Rong, Y.-Y. Li, Porous NiTi alloy prepared from elemental powder sintering, J. Mater. Res. 13 (1998) 2847–2851, https://doi.org/10.1557/JMR.1998.0389.
[26] M.H. Elahinia, M. Hashemi, M. Tabesh, S.B. Bhaduri, Manufacturing and processing of NiTi implants: a review, Prog. Mater. Sci. 57 (2012) 911–946, https://doi.org/10.1016/j.pmatsci.2011.11.001.
[27] M. Bram, A. Ahmad-Khanlou, A. Heckmann, B. Fuchs, H.P. Buchkremer, D. Stöver, Powder metallurgical fabrication processes for NiTi shape memory alloy parts, Mater. Sci. Eng. A 337 (2002) 254–263, https://doi.org/10.1016/S0921-5093(02)00028-X.
[28] M.K. Stanford, W.A. Wozniak, T.R. McCue, Addressing machining issues for the intermetallic compound 60-NITINOL. https://ntrs.nasa.gov/citations/20140007272, 2012 (accessed November 25, 2025).
[29] Y.Q. Fu, Y.W. Gu, C. Shearwood, J.K. Luo, A.J. Flewitt, W.I. Milne, Spark plasma sintering of TiNi nano-powders for biological application, Nanotechnology 17 (2006) 5293–5298, https://doi.org/10.1088/0957-4484/17/21/002.
[30] J. Butler, P. Tiernan, A.A. Gandhi, K. McNamara, S.A.M. Tofail, Production of nitinol wire from elemental nickel and titanium powders through spark plasma sintering and extrusion, J. Mater. Eng. Perform. 20 (2011) 757–761, https://doi.org/10.1007/s11665-011-9837-z.
[31] J. Mentz, M. Bram, H.P. Buchkremer, D. Stöver, Improvement of mechanical properties of powder metallurgical NiTi shape memory alloys, Adv. Eng. Mater. 8 (2006) 247–252, https://doi.org/10.1002/adem.200500258.
[32] G.A. Yurko, J.W. Barton, J.G. Parr, The crystal structure of Ti2Ni, Acta Crystallogr. 12 (1959) 909–911, https://doi.org/10.1107/S0365110X59002559.
[33] Ti2Ni Crystal structure - SpringerMaterials, (n.d.). https://materials.springer.com/isp/crystallographic/docs/sd_1818075 (accessed November 25, 2025).
[34] S.L. Zhu, X.J. Yang, D.H. Fu, L.Y. Zhang, C.Y. Li, Z.D. Cui, Stress–strain behavior of porous NiTi alloys prepared by powders sintering, Mater. Sci. Eng. A 408 (2005) 264–268, https://doi.org/10.1016/j.msea.2005.08.012.
[35] A.R. Pelton, in: Proceedings of SMST-94: the First International Conference on Shape Memory and Superelastic Technologies : March 7-10, 1994, Asilomar Conference Center, Pacific Grove, California, MIAS, Monterey, CA, 1995.
[36] T. Mousavi, F. Karimzadeh, M.H. Abbasi, Synthesis and characterization of nanocrystalline NiTi intermetallic by mechanical alloying, Mater. Sci. Eng. A 487 (2008) 46–51, https://doi.org/10.1016/j.msea.2007.09.051.
[37] B. Bertheville, M. Neudenberger, J.-E. Bidaux, Powder sintering and shape-memory behaviour of NiTi compacts synthesized from Ni and TiH2, Mater. Sci. Eng. A 384 (2004) 143–150, https://doi.org/10.1016/j.msea.2004.06.025.
[38] J.-E. Bidaux, A. Jochem, D. Zufferey, E. Carreno-Morelli, Metal injection moulding of NiTi shape memory alloys, Eur. Powder Metall. Conf. 2 (2007) 223–228.
[39] H. Li, B. Yuan, Y. Gao, C.Y. Chung, M. Zhu, High-porosity NiTi superelastic alloys fabricated by low-pressure sintering using titanium hydride as pore-forming agent, J. Mater. Sci. 44 (2009) 875–881, https://doi.org/10.1007/s10853-008-3193-x.
[40] H.H. Mohd Zaki, M. SHOLIHIN, J. Abdullah, N. SARIFUDDIN, Comparison studies on phase formation and transformation behavior between Ni-Ti and Ni-TiH2 synthesized via solid State sintering, Int. J. Curr. Res. Sci. Eng. Technol. 1 (2018) 464, https://doi.org/10.30967/ijcrset.1.S1.2018.464-470.
[41] B. Sharma, S.K. Vajpai, K. Ameyama, An efficient powder metallurgy processing route to prepare high-performance β-Ti–Nb alloys using pure titanium and titanium hydride powders, Metals 8 (2018) 516, https://doi.org/10.3390/met8070516.
[42] B. Sharma, Y. Shogo, M. Kawabata, S.K. Vajpai, K. Ameyama, Fabrication of Ti from a blend of Ti and TiH2 powders via powder metallurgy processing, Mater. Manuf. Process. 34 (2019) 1745–1752, https://doi.org/10.1080/10426914.2019.1669802.
[43] A. Weiser, J. Todt, J. Holcova, T. Zalezak, A.M. Paulik, D. Holec, M. Jary, O. Zobac, J. Mrazek, J. Frenzel, J. Keckes, A. Dlouhy, Hydrogen penetration into the NiTi superelastic alloy investigated in-situ by synchrotron diffraction experiments, Acta Mater. 277 (2024) 120217, https://doi.org/10.1016/j.actamat.2024.120217.
[44] Y. Fukai, The Metal-Hydrogen System: Basic Bulk Properties, Springer, Berlin, Heidelberg, 2005, https://doi.org/10.1007/3-540-28883-X.
[45] DynTHERM – Hochdruck-TGA - TA instruments. https://www.tainstruments.com/dyntherm/?lang=de, 2017 (accessed October 22, 2024).
[46] S.L. Wei, Y. Ma, D. Raabe, Reactive vapor-phase dealloying-alloying turns oxides into sustainable bulk nano-structured porous alloys, Sci. Adv. 10 (2024) eads2140, https://doi.org/10.1126/sciadv.ads2140.
[47] A. San-Martin, F.D. Manchester, The H−Ti (Hydrogen-Titanium) system, Bull. Alloy Phase Diagr. 8 (1987) 30–42, https://doi.org/10.1007/BF02868888.
[48] C. Jiménez, F. Garcia-Moreno, B. Pfretzschner, M. Klaus, M. Wollgarten, I. Zizak, G. Schumacher, M. Tovar, J. Banhart, Decomposition of TiH2 studied *in situ* by synchrotron X-ray and neutron diffraction, Acta Mater. 59 (2011) 6318–6330, https://doi.org/10.1016/j.actamat.2011.06.042.
[49] S. Fukada, M. Nishikawa, Semi-empirical equations for pressure-composition-temperature curves of the Ti-H system, J. Alloys Compd. 209 (1994) L23–L27, https://doi.org/10.1016/0925-8388(94)91066-9.
[50] K.V. Manukyan, A.G. Avetisyan, C.E. Shuck, H.A. Chatilyan, S. Rouvimov, S. L. Kharatyan, A.S. Mukasyan, Nickel oxide reduction by hydrogen: kinetics and structural transformations, J. Phys. Chem. C 119 (2015) 16131–16138, https://doi.org/10.1021/acs.jpcc.5b04313.
[51] A.M. Padhan, S. Hajra, J. Kumar, M. Sahu, S. Nayak, H. Khanbareh, H.J. Kim, P. Alagarsamy, NiO–Ti nanocomposites for contact electrification and energy harvesting: experimental and DFT+U studies, Sustain. Energy Fuels 6 (2022) 2439–2448, https://doi.org/10.1039/D2SE00246A.
[52] R. Li, P. Niu, S. Deng, T. Yuan, G. Liu, Diffusivity of Ti-Ni diffusion couple enhanced by pulse current during spark plasma sintering, Metall. Mater. Trans. B 51 (2020) 6–10, https://doi.org/10.1007/s11663-019-01725-7.
[53] D.G. Morris, M.A. Morris, NiTi intermetallic by mixing, milling and interdiffusing elemental components, Mater. Sci. Eng. A 110 (1989) 139–149, https://doi.org/10.1016/0921-5093(89)90165-2.
[54] J. Laeng, Z. Xiu, X. Xu, X. Sun, H. Ru, Y. Liu, Phase formation of Ni–Ti via solid state reaction, Phys. Scr. T129 (2007) 250–254, https://doi.org/10.1088/0031-8949/2007/T129/056.
[55] H. Sekimoto, T. Uda, Y. Nose, S. Sato, H. Kakiuchi, Y. Awakura, Reduction of titanium oxide in the presence of nickel by nonequilibrium hydrogen gas, J. Mater. Res. 24 (2009) 2391–2399, https://doi.org/10.1557/jmr.2009.0286.
[56] V.G. Chuprina, I.M. Shalya, Reactions of TiNi with oxygen, Powder Metall. Met. Ceram. 41 (2002) 85–89, https://doi.org/10.1023/A:1016020800727.
[57] J. Frenzel, E.P. George, A. Dlouhy, C.H. Somsen, M.F.-X. Wagner, G. Eggeler, Influence of Ni on martensitic phase transformations in NiTi shape memory alloys, Acta Mater. 58 (2010) 3444–3458, https://doi.org/10.1016/j.actamat.2010.02.019.
[58] M. Kuběnová, J. Záležák, J. Čermák, A. Dlouhý, Impact of hydrogen-assisted heat treatments on microstructure and transformation path in a Ni-rich NiTi shape memory alloy, J. Alloys Compd. 577 (2013) S287–S290, https://doi.org/10.1016/j.jallcom.2012.07.096.
[59] M.V. Zimmermann, O. Ivashko, F. Saldaña, et al., P21.1 at PETRA III – a high-energy X-ray diffraction beamline for physics and chemistry, J. Synchrotron. Radiat. 32 (3) (2025) 802–814, https://doi.org/10.1107/S1600577525002826.